
Research Article: New Research | Disorders of the Nervous System

***In vivo* diffusion tensor imaging in acute and subacute phases of mild traumatic brain injury in rats**

<https://doi.org/10.1523/ENEURO.0476-19.2020>

Cite as: eNeuro 2020; 10.1523/ENEURO.0476-19.2020

Received: 10 November 2019

Revised: 27 April 2020

Accepted: 11 May 2020

This Early Release article has been peer-reviewed and accepted, but has not been through the composition and copyediting processes. The final version may differ slightly in style or formatting and will contain links to any extended data.

Alerts: Sign up at www.eneuro.org/alerts to receive customized email alerts when the fully formatted version of this article is published.

Copyright © 2020 San Martín Molina et al.

This is an open-access article distributed under the terms of the Creative Commons Attribution 4.0 International license, which permits unrestricted use, distribution and reproduction in any medium provided that the original work is properly attributed.

Manuscript Title Page

1

2 1. Manuscript title3 *In vivo* diffusion tensor imaging in acute and subacute phases of mild traumatic brain injury in rats.

4

5 2. Abbreviated title

6 DTI in acute and subacute after mTBI in rats

7

**8 3. List of all Author Names and Affiliations in order as they would appear in the
9 published article**10 Isabel San Martín Molina¹, Raimo A. Salo¹, Ali Abdollahzadeh¹, Jussi Tohka¹, Olli Gröhn¹, and
11 Alejandra Sierra¹12 ¹A.I. Virtanen Institute for Molecular Sciences, University of Eastern Finland, PO 1627, FI-70211 Box
13 Kuopio, Finland**14 4. Author contributions**15 I.S.M.M., O.G., and A.S designed the experiment; I.S.M.M. performed the experiments; I.S.M.M.,
16 R.S., A.A., analyzed data; I.S.M.M., R.S., A.A., J.T., O.G., and A.S. wrote the paper.

17

18 5. Correspondence should be addressed to19 Alejandra Sierra, PhD. E-mail: alejandra.sierralopez@uef.fi

20 A.I. Virtanen Institute for Molecular Sciences

21 University of Eastern Finland (Kuopio Campus)

22 PO Box 1627 (Street address: Neulaniementie 2)

23 FI-70211 Kuopio, Finland

24 Tel. +358 40 355 2219

25 Fax. +358 17 163 030

26 E-mail: alejandra.sierralopez@uef.fi

27

28 6. Number of figures

29 9 figures

30 7. Number of tables

31 2 tables

32 8. Number of Multimedia

33 None

34 9. Number of words for Abstract

35 250 words

36 **10. Number of words for Significance Statement**

37 119 words

38 **11. Number of words for Introduction**

39 508 words

40 **12. Number of words for Discussion**

41 2184 words

42 **13. Acknowledgements**

43 We thank Ms. Maarit Pulkkinen for her assistance in animal handling and histologic procedures,
44 and Karthik Chary for his assistance with the *in vivo* MRI data collection.

45

46 **14. Conflict of Interest**

47 The authors declare no competing financial interests

48 **15. Funding sources**

49 This study was supported by the Academy of Finland (#275453 and #312686).

50

51

52

53

54

55

56

57

58

59

60

61

62

63 **Abstract**

64 Mild traumatic brain injury (mTBI) is the most common form of TBI with 10-25% of the patients
65 experiencing long-lasting symptoms. The potential of diffusion tensor imaging (DTI) for evaluating
66 microstructural damage after TBI is widely recognized, but the interpretation of DTI changes and
67 their relationship with the underlying tissue damage is unclear. We studied how both axonal
68 damage and gliosis contribute to DTI alterations after mTBI. We induced mTBI using the lateral
69 fluid percussion injury model in adult male Sprague-Dawley rats, and scanned them at 3 and 28
70 days post-mTBI. To characterize the DTI findings in the tissue, we assessed the histology by
71 performing structure tensor-based analysis and cell counting on myelin- and Nissl-stained sections,
72 respectively. In particular, we studied the contribution of two tissue components, myelinated
73 axons and cellularity, to the DTI changes. Fractional anisotropy (FA), mean diffusivity (MD), and
74 axial diffusivity (AD) were decreased in both white and grey matter areas in the acute phase post-
75 mTBI, mainly at the primary lesion site. In the subacute phase, FA and AD were decreased in the
76 white matter, external capsule, corpus callosum, and internal capsule. Our quantitative histologic
77 assessment revealed axonal damage and gliosis throughout the brain in both white and grey
78 matter, consistent with the FA and AD changes. Our findings suggest that the usefulness of *in vivo*
79 DTI is limited in its detection of secondary damage distal to the primary lesion, while at the lesion
80 site, DTI detected progressive microstructural damage in the white and grey matter after mTBI.

81

82 **Key words:** diffusion tensor imaging; mild traumatic brain injury; structure tensor; axonal damage;
83 cell counting; inflammation; secondary damage.

84

85 **Significance statement**

86 Mild traumatic brain injury (mTBI) is a major health problem worldwide with an unclear diagnosis.
87 Using the lateral fluid percussion injury model in rats, we induced mTBI to assess the potential of
88 *in vivo* diffusion tensor imaging (DTI) for non-invasively detecting progressive microstructural
89 tissue damage. To interpret the changes observed in DTI, we performed extensive quantitative
90 histologic assessment of the tissue microstructure. From the acute to subacute phases after mTBI,
91 *in vivo* DTI detected progressive microstructural tissue alterations in the white and grey matter
92 associated with axonal damage and gliosis. Although *in vivo* DTI failed to detect secondary tissue
93 damage far from the primary lesion, these findings provide new insights for detecting mild tissue
94 damage using *in vivo* DTI.

95

96 **Introduction**

97 Mild traumatic brain injury (mTBI) is the most common form of TBI, affecting 42 million people
98 worldwide per year (Gardner and Yaffe, 2015). Clinically, mTBI is defined as a mild insult to the
99 head causing a brief (< 30 min) period of unconsciousness and/or confusion and disorientation
100 (Arciniegas et al., 2005; McInnes et al., 2017). Because of the absence of physical signs of severe
101 injury, most mTBI patients are discharged without follow-up (Mayer et al., 2017). However,
102 approximately 10-25% of the patients with mTBI suffer long-term consequences such as
103 depression, attention or memory problems, and sleep or mood disorders, which still persist one
104 year after the injury (Grandhi et al., 2017).

105 Computed tomography (CT) and MRI are the gold-standard techniques for clinically assessing
106 tissue damage after TBI (Kim and Gean, 2011). CT is commonly available and used in the acute
107 phase of TBI for initial assessment of the damage severity (Mutch et al., 2016). Currently, MRI
108 methods such as T1- and T2-weighted, susceptibility-weighted imaging, and diffusion-weighted
109 imaging are used in routine clinical practice in both acute and chronic phases of head injury

110 (Amyot et al., 2015). These MRI methods are sensitive to macroscopic damage such as
111 parenchymal bleeding, edema, and penetrating injuries after moderate and severe TBI (Kim and
112 Gean, 2011; Kinnunen et al., 2011). CT and conventional MRI approaches fail to detect widespread
113 microscopic injuries such as axonal injury, however, which is commonly observed after mTBI in
114 humans (Shenton et al., 2012) and characterized histologically in animals (Johnson et al., 2013).

115 Diffusion tensor imaging (DTI) (Basser et al., 1994; Mori and Zhang, 2006) is widely used in
116 experimental and clinical settings to investigate TBI due to its sensitivity to changes in the tissue
117 microstructure (Pierpaoli et al., 1996; Sidaros et al., 2008; Laitinen et al., 2015; Sierra et al., 2015;
118 Hutchinson et al., 2018; Tae et al., 2018). Several experimental *in vivo* DTI studies have
119 characterized microstructural changes mainly in the acute phase of mTBI (Budde et al., 2013; Long
120 et al., 2015; Wright et al., 2016; Li et al., 2016). The interpretation of changes in DTI metrics as an
121 indicator of changes in the cellular level, however, is ambiguous. Only a few studies have
122 combined DTI and histology, but only qualitative histologic analysis was applied with no direct link
123 to the DTI metrics (Zhuo et al., 2012; Hylin et al., 2013; Singh et al., 2016; Tu et al., 2017; Herrera
124 et al., 2017).

125 The aim of this study was to identify the spatial distribution of tissue damage throughout the
126 rat brain in the acute and subacute phases of mTBI using *in vivo* MRI. As screening methods, we
127 used *in vivo* voxel-wise and deformation-based morphometry analyses for DTI and T2-weighted
128 MRI data, respectively, to assess progressive microstructural alterations and local morphologic
129 volumetric changes throughout the brain. To interpret DTI changes in the tissue microstructure,
130 we applied a structure tensor (ST) analysis for myelin-stained sections and an automated cell
131 counting method for Nissl-stained sections to examine the contribution of both myelinated axons
132 and cellularity to the DTI parameters.

133

134 **Materials and methods**

135 **Animals.** Adult male Sprague-Dawley rats (n = 25, 10 weeks old, weight 300–450 g, Harlan
136 Netherlands B.V., Horst, Netherlands) were used in all the experiments. All the animals were
137 housed individually in cages and maintained in a climate-controlled room (temperature $22 \pm 1^\circ\text{C}$,
138 air humidity 50%-60%) with a 12-h light/dark cycle and an *ad libitum* diet. All the experimental
139 procedures were approved by the Animal Ethics Committee of the Provincial Government of
140 Southern Finland and conducted in accordance with the guidelines set by the European Union
141 Directives 2010/63/EU.

142 **Animal model of mild TBI.** We induced mTBI using the lateral fluid percussion (LFP) injury model,
143 as described previously (Kharatishvili et al., 2006). Briefly, rats were anesthetized by
144 intraperitoneal injection (6 ml/kg) of a mixture of sodium pentobarbital (58 mg/kg), chloral
145 hydrate (60 mg/kg), magnesium sulfate (127.2 mg/kg), propylene glycol (42.8%), and absolute
146 ethanol (11.6%). We then performed a craniotomy (5-mm diameter) between bregma and lambda
147 on the left convexity (anterior edge 2.0 mm posterior to bregma; lateral edge adjacent to the left
148 lateral ridge). LFP injury was induced (n = 13) by a transient fluid pulse impact (21–23 ms) against
149 the exposed dura using a fluid percussion device (AmScien Instruments, Richmond, VA, USA). The
150 impact pressure was adjusted to induce a mild brain injury (0.88 ± 0.21 atm). After the impact, we
151 removed the animals from the fluid percussion device, and assessed the temporary absence of
152 spontaneous breathing by measuring the apnea time. Additionally, we assessed the right-time
153 reflex latency, presence of hematoma on the impact site and seizure post-mTBI. Sham-operated
154 control animals (n = 12) underwent the same surgical procedures without the impact. Mild TBI
155 animals recover same as the sham-operated animals after the impact, with no apnea, hematoma
156 or post-injury seizure. We also did not observe differences in right-time reflex latency in mTBI

157 animals when comparing to sham-operated animals. The mortality during our experiments was
158 0%.

159 ***In vivo* MRI.** All rats were scanned *in vivo* on days 3 and 28 after the injury under 1.0%–1.5%
160 isoflurane (in 70% nitrogen/30% oxygen) anesthesia. We performed *in vivo* imaging using a
161 horizontal 7 T Bruker PharmaScan MRI system with an actively decoupled quadrature volume
162 transmitter coil and a quadrature receiver surface coil pair (Bruker Biospin, Ettlingen, Germany).
163 We monitored the breathing and temperature of the rats during the scans using a respiration
164 pneumatic sensor and a rectal temperature probe, maintaining physiologic stability (breathing
165 approximately at 60 bpm, temperature ~37°C) with a water circulation system (ThermoFisher
166 Scientific, Loughborough, England). *In vivo* DTI data were acquired using three-dimensional (3D)
167 spin echo-planar imaging sequences with respiratory gating and the following parameters:
168 repetition time = 1000 ms, echo time = 30 ms, number of averages = 1, field of view = 21.4 × 14.4 ×
169 15.6 mm³, bandwidth = 300 kHz, matrix size = 142 × 96 × 52, b0 images = 4, 60 directions (δ = 4
170 ms, Δ = 11 ms, b-value = 2000 s/mm²) with a resolution = 0.15 × 0.15 × 0.30 mm³, and a scan time
171 of 2–3 h. We acquired T2-weighted images using two-dimensional (2D) fast spin-echo sequences
172 with the following parameters: repetition time = 7800 ms, echo time = 40 ms, rapid acquisition
173 relaxation enhancement factor = 8, number of averages = 8, field of view = 2.56 × 2.56 cm², matrix
174 size = 170 × 342, resolution = 75 × 150 μ m², number of slices = 52, slice thickness = 300 μ m, and
175 scan time = 22 min.

176 **Statistical analyses of *in vivo* MRI.**

177 In voxel-wise and deformation-based morphometry analyses, we used FSL randomize (Winkler et
178 al., 2014) with 10000 permutations and threshold-free cluster enhancement (TFCE)(3D-
179 connectivity with standard parameters) to perform the statistical analyses. We used the

180 permutation-based TFCE (Smith and Nichols, 2009) with the default parameters ($H = 2$, $E = 0.5$, $C =$
181 6), which performs family-wise error (FWE) multiple comparison correction to the cluster-
182 enhanced statistic values. For further discussion how to interpret TFCE results, we refer to (Smith
183 and Nichols, 2009; Noble et al., 2020).

184 ***In vivo* MRI data analysis.** For DTI analysis, we first converted the DTI data to Nifti format. Second,
185 we pre-processed and performed all the analyses using tools in FMRIB Software Library (FSL 5.0.9;
186 <http://www.fmrib.ox.ac.uk/fsl/>). Then, we performed simultaneous multiple correction for motion
187 and eddy current distortions with the FSL eddy tool (Andersson and Sotiropoulos, 2016). For that,
188 we used eddy unchanged parameters without the opposite phase encoding correction (topup).
189 After eddy current corrections, we determined the diffusion tensors, and the respective
190 eigenvalues (λ_1 , λ_2 , and λ_3) of the diffusion tensors were calculated using FSL. We then generated
191 fractional anisotropy (FA), axial diffusivity (AD), radial diffusivity (RD), and mean diffusivity (MD)
192 maps (Pajevic and Pierpaoli, 1999). We also calculated linear (CL), planar (CP), and spherical (CS)
193 anisotropy indices (Westin et al., 2002).

194 To determine the differences between the animal groups, we performed a voxel-wise statistical
195 analysis of the whole brain between sham-operated and mTBI animals at both time-points. We
196 created a study-specific FA template (the mean of 5 accurately registered sham-operated brain
197 images). The template was then used in the affine and nonlinear (symmetric image normalization
198 method (SyN; Avants et al., 2008) co-registration of sham-operated and mTBI brain images from
199 both time-points using Advanced Normalization Tools (ANTs;
200 <http://stnava.github.io/ANTs/>)(Avants et al., 2011).

201 Additionally, based on the voxel-wise statistical analysis results on days 3 and 28 after injury,
202 we used an ROI approach to correlate DTI data with the histologic analyses, selecting the same
203 subgroup of animals used for the histologic procedures. In that subgroup, we manually outlined

204 different brain areas at three different brain levels: two levels rostral to the lesion site, +1.08 and -
205 1.60 mm from bregma, and one at the level of the lesion, -3.60 mm from bregma. We selected
206 these three levels based on the absence or presence of major statistically significant differences in
207 the DTI group analysis described above. The brain areas included in the ROI analysis were the ipsi-
208 and contralateral corpus callosum, external capsule, layer VI of somatosensory cortex, internal
209 capsule, and ventral posterolateral thalamic nucleus (**Fig. 1**). From each ROI, we extracted the FA
210 and AD on day 28 post-mTBI as the only DTI parameters with statistically significant differences at
211 this time-point. The ROIs were outlined on FA maps from each individual animal using in-house
212 Matlab code (AEDES, <http://aedes.uef.fi/>; Matlab R2012b).

213 T2-weighted data were analyzed using deformation-based morphometry to assess local
214 morphologic volume differences throughout the brain (Gaser et al., 2001). We created a study-
215 specific T2-weighted template image (the mean of 6 accurately registered sham-operated and
216 mTBI brain images). Then, the individual images were co-registered to the template using ANTs
217 linear and non-linear SyN registration. To determine the changes in each voxel, we computed the
218 Jacobian determinant by the inverse displacement vector field from the SyN registration using the
219 CreateJacobianDeterminantImage script of ANTs. In this analysis, we compared sham-operated
220 and mTBI rats on days 3 and 28 using FSL randomize.

221 At 3 days post-mTBI, we observed that the *in vivo* T2-weighted and DTI data showed blood-
222 related susceptibility difference-artifacts related to the surgical procedure in seven sham-operated
223 and mTBI animals, preventing satisfactory co-registration of some brain volumes for the T2-
224 weighted deformation-based morphometry and DTI voxel-wise statistical analyses. From the 25
225 animals mentioned above ($n_{\text{total}} = 25$), we excluded 6 animals from the T2-weighted analysis ($n =$
226 19), and 7 animals from the *in vivo* DTI analysis on day 3 post-mTBI ($n = 18$). For the same reason,

227 on day 28 post-mTBI, we excluded three animals from the T2-weighted data analysis (n = 22), and
228 two animals from the *in vivo* DTI analysis (n = 23).

229 **Tissue processing and histology.** Thirty-five days post-mTBI, we anesthetized all rats with an
230 intraperitoneal injection of urethane (1.25 g/kg, ip, Sigma-Aldrich, Helsinki, Finland). Next, the
231 animals were transcardially perfused with 0.9% NaCl for 5 min (30 ml/min), followed by 4%
232 paraformaldehyde in 0.1 M PB pH 7.4 for 25 min (30 ml/min). The brains were removed from the
233 skull and post-fixed in 4% PFA for 4 h. The brains were then placed in a cryoprotective solution
234 (20% glycerol in 0.02 M potassium phosphate-buffered saline, pH 7.4) for 36 h. After
235 cryoprotection, we rapidly froze the brains in dry ice and stored them at -70°C until cutting. Using
236 a sliding microtome, we sectioned a subgroup of brains (sham-operated = 6; mTBI = 8) in the
237 coronal plane (30 µm, 1-in-5 series). We stored the first series of sections in 10% formalin, and the
238 remaining series in cryoprotectant tissue-collecting solution (30% ethylene glycol, 25% glycerol in
239 0.05 M sodium phosphate buffer) at -20°C until histologic processing.

240 For the first series of sections, we performed Nissl staining (thionin) to assess the
241 cytoarchitectonics, gliosis (increased cell density), and neurodegeneration after mTBI. In the
242 second series of sections, we used gold chloride (Laitinen et al., 2010) to assess the
243 myelinoarchitecture, myelin content, and axonal damage of the brain areas affected after mTBI.
244 Briefly, sections mounted on gelatin-coated slides were incubated in 0.2% gold chloride solution
245 (HAuCl₄·3H₂O, G-4022 MilliporeSigma, St Louis, MO, USA) in 0.02 M sodium phosphate buffer (pH
246 7.4) containing 0.09% NaCl for 3-4 h at room temperature in the dark. We then washed the slides
247 twice (4 min each) in 0.02 M sodium phosphate buffer containing 0.09% NaCl, and incubated them
248 in 2.5% sodium thiosulfate solution (5 min). After three washes in the buffer solution (10 min

249 each), the slides were dehydrated (13 min), cleared in xylene (15 min), and cover-slipped with
250 DePeX (Merck Millipore, Germany).

251 **Structure tensor (ST) analysis of myelin-stained sections.** For the ST analysis, high-resolution
252 photomicrographs of myelin-stained sections were acquired at a resolution of $0.013 \mu\text{m}^2/\text{pixel}$
253 using a light microscope (Zeiss Axio Imager2, White Plains, NY, USA) equipped with a digital
254 camera (Zeiss Axiocam color 506). Each photomicrograph was analyzed using the ST-based
255 method (Budde and Frank, 2012). To derive the anisotropy from the image, we used pixelwise ST
256 analysis, where directional derivatives of an image were first produced by convolving the image
257 with the directional derivative of a 2D Gaussian function (size = 11 pixels, $\sigma = 3$ pixels). Then, the
258 structure tensor for each image pixel was formed from the derivatives. These structure tensors
259 were summed into a pixelwise structure tensor within a 128×128 pixel window, and the pixelwise
260 tensor was eigen-decomposed. We used the eigenvalues to calculate the anisotropy index (AI). To
261 compare the AI derived from ST-based analysis to the FA derived from DTI, we performed similar
262 ROI analyses of the DTI data on myelin-stained sections, selecting the same brain areas at the
263 locations mentioned above for the DTI data (**Fig. 1**). In the multiple linear regression analyses, we
264 correlated MRI and histological parameters obtained from white and grey matter areas
265 individually, and also using combinations of connected white and grey matter areas.

266 **Cell density (CD) analysis on Nissl-stained sections.** We acquired high-resolution
267 photomicrographs of the Nissl-stained sections, and analyzed all the images using an in-house
268 Matlab code for automated cell counting analysis. Briefly, we developed an automated cell
269 counting technique based on preliminary foreground segmentation and a subsequent
270 segmentation error-correction strategy. For the preliminary cell segmentation, we applied Chan-
271 Vese active contours (Chan and Vese, 2001) as implemented in Matlab. The Chan-Vese model was

272 initialized with a random binary mask. The speed function was the gradient of the green channel
273 of the RGB images; the cell membranes appeared sharper in the green channel than in the blue
274 and red channels. We set the smooth factor equal to 0.2, and the maximum number of iterations
275 to 300 to perform the segmentation. The initial contours were deformed on the speed function to
276 adapt to the cell shape, resulting in the preliminary segmentation of cells. The preliminary
277 segmentation, however, contained under-segmented components (cells touching each other
278 appear in the same connected component) and very small noise components. Thus, we fitted an
279 ellipse to every preliminary component. If the major axis of an ellipse was smaller than a threshold
280 [$S = 30$] the component was discarded, and if the major axis was greater than a threshold [$B = 140$]
281 the component was recognized as an under-segmented component. The preliminary segmented
282 components with the major axis of the fitted ellipse in [S, B] were correctly segmented, requiring
283 no further analysis. We ran a secondary segmentation on every preliminary under-segmented
284 component using the marker-based watershed transform. We determined the markers by first
285 Gaussian filtering the intensity image obtained from the HSV transform of the RGB image. Within
286 the domain of an under-segmented component, we defined the regional maxima of the H-maxima
287 transform of the filtered image as markers. We applied a set of conditions to the extracted
288 markers: 1) the value of a marker on the intensity image should be greater than a threshold [$I =$
289 0.5]; 2) the spatial distance between two markers should be greater than a threshold [$D_s = 70$];
290 and 3) the intensity distance between two markers should be greater than a threshold [$D_i = 1$].
291 Determining the set of markers, we applied a watershed transform to finalize the cell
292 segmentation. We set the thresholds to experimentally evaluate the performance of the
293 automated cell segmentation compared with 10 images in which all cells were counted by an
294 expert (ISMM). We used the same threshold values for all images from different brain regions and

295 experimental conditions. We defined the cell density as $\rho = N/A$, where N is the number of cells in
296 the ROI and A is the area of the ROI.

297 **Statistical analyses of the histology.** ROIs statistical analyses of ST and CD histologic parameters
298 were performed with GraphPad Prism (Version 5.03, GraphPad Software Inc., La Jolla, CA, USA). All
299 values were expressed as mean \pm standard deviation. The unpaired t-test was used to assess
300 differences between both sham-operated and mTBI animals. Multiple linear regression was used
301 to assess the relationship between DTI (FA and AD) and the histologic (AI and CD) parameters
302 (regression model: DTI parameter \sim AI + CD). Multiple comparison correction was applied based on
303 false discovery rate (FDR) using Benjamini-Hochberg procedure (Benjamini and Hochberg, 1995).
304 To provide more information than just significant and non-significant division, we computed FDR-
305 adjusted p -values that we call q -values according to the usual terminology. The FDR-adjustment
306 was performed using the standard procedure introduced by Yekutieli and Benjamini (1999)
307 (Yekutieli and Benjamini, 1999). We applied the FDR to correct for multiple comparisons
308 separately in the unpaired t-test and the multiple linear regression p -values. The threshold for
309 statistical significance was set to $q < 0.05$.

310

311 **Results**

312 Three days after the injury, 8 of 13 mTBI rats showed hyperintensity indicative of edema at the
313 injury site in the somatosensory cortex at -3.60 mm from bregma on T2-weighted images.
314 Additionally, two of these eight rats also showed hypointensity in the cortex, indicating the
315 presence of bleeding. In the subacute phase, 6 of 13 rats showed persistent cortical edema, but it
316 was less pronounced compared with that at 3 days post-mTBI. Three of these six rats also showed
317 bleeding.

318 **Whole-brain voxel-wise group analysis of *in vivo* DTI in the acute phase of mTBI**

319 At day 3 post-mTBI, voxel-wise group analysis revealed a decrease in the DTI parameters in both
320 the grey and white matter, mainly ipsilateral to the injury. Rostrally, at -1.60 mm from bregma, we
321 observed significant differences between the sham-operated and mTBI groups (**Fig. 2**). At this
322 level, we observed significant decreases in FA, AD, and MD along the external capsule up to the
323 cingulum. The AD and MD were significantly different between groups in the white matter,
324 including the corpus callosum and fimbria, and in the grey matter in the somatosensory cortex,
325 whereas differences in RD were only observed in the somatosensory cortex (**Fig. 2**). At the
326 epicenter of the lesion, at -3.60 mm, FA, AD, and MD were decreased in white matter areas: the
327 external capsule, corpus callosum, internal capsule, and cingulum. In grey matter areas, all the
328 parameters were decreased in the somatosensory cortex, auditory cortex, and hippocampus (**Fig.**
329 **2**). Also, CL and CS significantly differed between groups in the corpus callosum, external capsule,
330 internal capsule, and somatosensory cortex, whereas significant differences in CP were only
331 observed in the external capsule (**Fig. 3**). At -4.60 mm from bregma, in addition to the structures
332 mentioned at the previous level, the corpus callosum showed a significant ipsilateral decrease that
333 extended to the contralateral side. Furthermore, the ventrobasal complex was highlighted in the
334 FA, AD, CL, and CS analyses (**Figs. 2 and 3**). More caudally at -5.60 mm, FA, AD, and MD were
335 decreased in the external capsule, corpus callosum, and auditory cortex. AD was also decreased in
336 the hippocampus and midbrain. Similarly to the previous level, RD was only decreased in the
337 auditory cortex (**Fig. 2**). Furthermore, CL and CS exhibited significant differences in the corpus
338 callosum, external capsule, and auditory cortex, whereas significant differences in the CP were
339 only observed in the external capsule (**Fig. 3**).

340 **Whole-brain voxel-wise group analysis of *in vivo* DTI in the subacute phase of mTBI**

341 At day 28 post-mTBI, voxel-wise group analysis revealed a decrease in DTI parameters mainly in
342 the white matter ipsilateral to the injury. Overall, we observed no progression of the abnormalities
343 between days 3 and 28. Rostrally in the brain, the analysis showed significant differences between
344 groups at -1.60 mm from bregma (**Fig. 4**). At this level, the external capsule and cingulum
345 exhibited a decrease in FA, AD, CL, and CS (**Figs. 3 and 4**). At -3.60 mm, FA and AD were decreased
346 in the corpus callosum, cingulum, and external capsule. FA was also decreased in the internal
347 capsule and fimbria (**Fig. 4**). CL and CS were also significantly different between groups in the
348 corpus callosum, external capsule, cingulum, and internal capsule (**Fig. 3**). Caudally at -4.60 mm,
349 FA, AD, CL, and CS were significantly decreased in the external capsule and cingulum. In addition,
350 FA and CL were decreased in the corpus callosum ipsi- and contralaterally (**Figs. 3 and 4**). At -5.60
351 mm from bregma, FA, CL, and CS were decreased in the corpus callosum and external capsule.
352 Additionally, AD and CP exhibited significant differences in the external capsule (**Figs. 3 and 4**).

353 **T2-weighted deformation-based morphometry analysis after mTBI**

354 To examine the intensity differences in T2-weighted images between sham and mTBI groups, we
355 also performed intensity-based statistical analyses, and found no significant difference (p -value =
356 0.05, FWE-corrected TFCE-enhanced statistics).

357 At day 3, mTBI animals showed decreased volume contralaterally in the lateral ventricle in the
358 more rostral levels (**Fig. 5A**). At the epicenter of the lesion, the volume was increased in the
359 ipsilateral external capsule and layer VI of somatosensory cortex, and decreased in the ventrobasal
360 complex after mTBI. At -4.60 mm, mTBI animals exhibited decreased volume ipsilaterally in the
361 dorsolateral geniculate nucleus, and increased volume in the external capsule (**Fig. 5A**). Even at -
362 5.60 mm from bregma, we still observed an increased volume in the external capsule.

363 At day 28 post-mTBI (**Fig. 5B**), the volume changes ipsilateral to the injury were more
364 widespread compared with day 3 (**Fig. 5A**). In addition, the volume changes observed at day 3

365 were further progressed at day 28. Rostrally, mTBI animals exhibited decreased volume in the
366 corpus callosum, cingulum, and caudate putamen. At -1.60 mm from bregma, the volume was
367 decreased in the internal capsule, fimbria, and motor cortex (**Fig. 5B**). At -3.60 mm, mTBI animals
368 showed decreased volume in the internal capsule, dentate gyrus, somatosensory cortex, and
369 ventrobasal complex. At -4.60 mm, the volume was decreased in the cingulum, corpus callosum,
370 ventrobasal complex, and somatosensory and auditory cortex (**Fig. 5B**). At -5.60 mm from bregma,
371 mTBI animals exhibited decreased volume in the corpus callosum and dentate gyrus, and in the
372 somatosensory, auditory and visual cortices. At this level, the medial geniculate nuclei showed an
373 increased volume after mTBI.

374 **Qualitative and quantitative histologic assessment of myelin and Nissl-stained sections in the**
375 **subacute phase of mTBI**

376 For histologic assessment, we focused our analysis on areas highlighted in the group analyses,
377 including the corpus callosum, external capsule, layer VI of somatosensory cortex, internal
378 capsule, and ventral posterolateral thalamic nucleus both ipsi- and contralaterally. We analyzed
379 these areas at two levels rostral to the lesion (+1.08 and -1.60 mm from bregma), and at the
380 epicenter of the lesion (-3.60 mm from bregma) where the group analyses showed or did not show
381 statistically significant differences.

382 The most devastating consequence after TBI is diffuse axonal injury caused by rapid
383 acceleration/deceleration movements of the head (Marion et al., 2018). As a result, the axonal
384 cytoarchitecture changes, progressing from a disruption in axonal transport to axonal swelling,
385 secondary disconnection, and, finally, demyelination or Wallerian degeneration (Johnson et al.,
386 2013). The alterations in myelinated axons at 35 days after injury may correspond with injured or
387 degenerating axons, or demyelination.

388 Together with a qualitative examination of the histologic preparations, we performed
389 quantitative assessments in both ipsi- and contralateral hemispheres to compare sham-operated
390 (n = 6) and mTBI animals (n = 8) by using ST analysis and automated cell counting on myelin- and
391 Nissl stained sections at day 35 post-mTBI. The results of the analysis are summarized in **Table 1**.
392 We did not find any qualitative or quantitative differences when comparing histologic
393 preparations from the contralateral side of sham-operated and mTBI animals (**Table 1**). Here, we
394 focus our description on the comparison of the ipsilateral hemisphere between sham-operated
395 and mTBI animals.

396 Rostrally, at +1.08 mm, we observed alterations along myelinated axons in the ipsilateral
397 external capsule and somatosensory cortex after mTBI (**Fig. 6Cii and Dii**), with no changes in
398 cellularity (**Fig. 6Civ and Div**). Ipsilaterally in the corpus callosum, however, we observed no
399 changes in the myelin or cellularity between mTBI and sham-operated animals (**Fig. 6Bi-iv**). We did
400 not find significant differences between sham-operated and mTBI animals in any of these areas
401 (**Table 1**).

402 At -1.60 mm from bregma, we observed more pronounced tissue alterations than at +1.08 mm.
403 Here, mTBI animals showed mild axonal damage and gliosis in the corpus callosum (**Fig. 7Bii-iv**).
404 We observed axonal damage and gliosis after mTBI in the external capsule and the somatosensory
405 cortex (**Fig. 7C and Dii-iv**). Although, some values showed a trend, especially the external capsule
406 with lower AI and higher CD values comparing animal groups, we did not find significant
407 differences between sham-operated and mTBI animals in any of these areas (**Table 1**).

408 The analyzed areas showed more extensive alterations at the epicenter of the lesion than
409 rostrally. In the corpus callosum, we observed widespread axonal damage (**Fig. 8Bii**) and increased
410 cellularity (**Fig. 8Biv**) after mTBI, however, no significant differences were found in AI or CD when

411 comparing sham-operated and mTBI animals (**Table 1**). In addition to the pronounced and
412 widespread axonal damage, we observed a loss of myelinated axons and increased cellularity in
413 the ipsilateral external capsule and somatosensory cortex in mTBI animals (**Fig. 8C and Dii-iv**) as
414 compared with sham-operated animals (**Fig. 8C and Di-iii**). In the external capsule, we found a
415 significant decrease in AI ($t = 4.97$, $q\text{-value} = 1.76 \times 10^{-2}$) which corroborated the damage and loss
416 of myelinated axons, and a significant increase in CD ($t = 4.71$, $q\text{-value} = 1.76 \times 10^{-2}$) along with
417 gliosis when comparing mTBI and sham-operated animals (**Table 1**). In the somatosensory cortex,
418 we only found a significant increase in CD ($t = 4.01$, $q\text{-value} = 3.41 \times 10^{-2}$) corresponding with the
419 presence of gliosis after mTBI (**Table 1**). Furthermore, in the ipsilateral internal capsule and ventral
420 posterolateral thalamic nucleus, we observed axonal damage (**Fig. 8Eii and Fii**) and increased
421 cellularity (**Fig. 8Eiv and Fiv**) after mTBI. We found a significant increase in CD in the internal
422 capsule, indicative of gliosis in mTBI animals when comparing to sham-operated ($t = 4.23$, $q\text{-value}$
423 $= 3.41 \times 10^{-2}$) (**Table 1**).

424

425 **Multiple linear regression of DTI and histologic parameters**

426 We assessed the relationship between the DTI and histologic parameters from the ST and CD
427 analyses in white and grey matter using a multiple linear regression test. Our regression model
428 evaluated the contribution of two factors, AI and CD, to FA or AD (DTI parameter \sim AI + CD). **Table**
429 **2** summarizes the outcomes of the multiple linear regression test, which includes the statistics of
430 the model (R^2 adjusted and F-statistic), the t-statistics for AI and CD ($t(\text{AI})$ and $t(\text{CD})$) and the
431 corresponding q -values. **Figure 9** shows the most representative multiple linear regression results
432 between FA or AD and $\chi = \beta_{\text{AI}} \times \text{AI} + \beta_{\text{CD}} \times \text{CD}$, where β is the weighting value.

433 Rostrally, at +1.08 mm, we found a correlation between FA and χ ($R^2 = 0.68$, q -value = 2.30×10^{-12} ;
434 **Fig. 9A**) and AD and χ ($R^2 = 0.66$, q -value = 3.68×10^{-12} ; **Fig. 9B**) when combining the corpus
435 callosum and external capsule (**Table 2**). In these two brain areas, FA ($t = 5.10$, q -value = 2.24×10^{-5})
436 and AD ($t = 6.34$, q -value = 4.55×10^{-7}) were positively associated with AI. We also found positive
437 association between FA ($t = 6.28$, q -value = 5.09×10^{-7}) and AD ($t = 4.53$, q -value = 1.36×10^{-4}), and
438 CD (**Table 2**). Despite the positive association between DTI and histologic parameters with AI and
439 CD, we observed low influence of the injury in the correlations (**Fig. 9A and B**).

440 At -1.60 mm from bregma, FA correlated with χ in the corpus callosum ($R^2 = 0.51$, q -value = 2.13
441 $\times 10^{-4}$), while AD correlated with χ in the external capsule ($R^2 = 0.25$, q -value = 2.82×10^{-2}) (**Table**
442 **2**). When combining the corpus callosum and external capsule, FA correlated with χ ($R^2 = 0.33$, q -
443 value = 4.10×10^{-5} ; **Fig. 9C**) and AD with χ ($R^2 = 0.55$, q -value = 5.39×10^{-9} ; **Fig. 9D**) (**Table 2**). Also,
444 we found that both FA ($t = 5.39$, q -value = 8.90×10^{-6}) and AD ($t = 7.54$, q -value = 9.93×10^{-9}) were
445 positively associated with AI (**Table 2**). At this level, we observed a moderate influence of the
446 injury in the relationship between DTI and histologic parameters, mainly in the external capsule
447 (**Fig. 9C and D**).

448 At the epicenter of the lesion (-3.60 mm), we found a correlation between DTI and χ
449 parameters in both white and grey matter areas (**Table 2**). In the external capsule, both FA ($R^2 =$
450 0.72 , q -value = 4.55×10^{-7}) and AD ($R^2 = 0.69$, q -value = 1.11×10^{-6}) correlated with χ (**Table 2**). We
451 found that both FA ($t = 3.00$, q -value = 1.80×10^{-2}) and AD ($t = 4.54$, q -value = 4.35×10^{-4}) in the
452 external capsule were positively associated with AI (**Table 2**). Similarly, in the internal capsule, we
453 also found a correlation between FA and χ ($R^2 = 0.23$, q -value = 4.13×10^{-2}), and AD and χ ($R^2 =$
454 0.33 , q -value = 7.91×10^{-3}) (**Table 2**). We found that only AD ($t = 3.72$, q -value = 3.51×10^{-3}) was
455 positively associated with AI (**Table 2**). When combining the corpus callosum and external capsule,

456 FA ($R^2 = 0.53$, q -value = 1.04×10^{-08}) and AD ($R^2 = 0.48$, q -value = 1.25×10^{-7}) correlated with χ
457 (**Table 2**). Also, we showed that both FA (AI: $t = 5.02$, q -value = 2.79×10^{-05} ; CD: $t = -4.63$, q -value =
458 9.88×10^{-5}) and AD (AI: $t = 5.45$, q -value = 7.50×10^{-6} ; CD: $t = -3.17$, q -value = 8.09×10^{-3}) were
459 positively associated with both histologic parameters (**Table 2**). When combining the three white
460 matter areas, we found a correlation between FA ($R^2 = 0.51$, q -value = 3.68×10^{-12} ; **Fig. 9E**) and AD
461 ($R^2 = 0.33$, q -value = 3.15×10^{-7} ; **Fig. 9F**) with χ (**Table 2**). Here, FA ($t = -8.52$, q -value = 1.72×10^{-11})
462 was negatively associated with CD (**Table 1**). Moreover, AD was positively associated with AI ($t =$
463 5.44 , q -value = 3.78×10^{-6}) and negatively associated with CD ($t = -5.23$, q -value = 7.49×10^{-6})
464 (**Table 2**). At this level, we found high influence of the injury in the correlation between DTI and
465 histologic parameters as shown by the ipsilateral values of the three brain areas (**Fig. 9E and F**). In
466 grey matter, we found that FA ($R^2 = 0.39$, q -value = 4.83×10^{-6} ; **Fig. 9G**) and AD ($R^2 = 0.14$, q -value
467 = 1.99×10^{-2} ; **Fig. 9H**) correlated with χ when combining the somatosensory cortex and ventral
468 posterolateral thalamic nucleus. Both FA ($t = -5.12$, q -value = 2.21×10^{-5}) and AD ($t = -2.95$, q -value
469 = 1.47×10^{-2}) were negatively associated with AI (**Table 2**). Here, despite we found associations
470 between DTI and histologic parameters, the influence due to the injury in these correlations was
471 low (**Fig. 9G and H**).

472

473 Discussion

474 In the present study, we investigated the potential of *in vivo* DTI to detect progressive widespread
475 microstructural tissue alterations in white and grey matter areas throughout the brain after mTBI
476 in rats. We performed quantitative histologic characterization of the *in vivo* DTI findings to unveil
477 the underlying tissue processes associated with mTBI using ST and automated cell counting
478 analyses in the subacute phase of mTBI. The key findings of this study were: (1) microstructural

479 tissue alterations detected by voxel-wise analysis of DTI maps in white and grey matter areas
480 progressed from day 3 to day 28; (2) volume reductions occur in white and grey matter areas in
481 the subacute phase; (3) decreases in FA and AD are associated with axonal damage and gliosis in
482 the subacute phase of mTBI; and 4) although we found a strong correlation between DTI and
483 histologic parameters far from the lesion site, DTI was unable to detect mild axonal damage at this
484 level. The combination of MRI and histologic analyses increases our knowledge of the potential of
485 *in vivo* DTI to detect microstructural tissue changes in the brain after mTBI. This study may provide
486 a new window for detecting progressive mild microstructural tissue damage using *in vivo* DTI.

487 **Microstructural alterations in the brain after mTBI**

488 Three days after mTBI, our voxel-wise group analysis showed a decrease in FA, MD, AD, CL, and CS
489 in major white matter areas, such as the corpus callosum, external capsule, and internal capsule in
490 the ipsilateral hemisphere. Previous studies using *in vivo* DTI in a rat model of mTBI also reported
491 changes in FA, AD, MD, and RD in white matter tracts in the acute phase (Long et al., 2015; Wright
492 et al., 2016; Li et al., 2016; Tu et al., 2017; Herrera et al., 2017). Several studies report decreased
493 FA in the corpus callosum at days 1 and 2 post-mTBI in the mild controlled cortical impact model
494 (Long et al., 2015; Li et al., 2016; Tu et al., 2017), and increased RD (Long et al., 2015; Tu et al.,
495 2017). Tu and collaborators also reported decreased AD and increased MD in the corpus callosum
496 at day 1 post-mTBI (Tu et al., 2017). Further, using a mild impact acceleration model, Herrera and
497 collaborators reported increased FA and MD in the fimbria and internal capsule, and increased RD
498 in the fimbria at day 3 post-mTBI (Herrera et al., 2017). Their study also showed decreased AD in
499 the genu of the corpus callosum and fimbria, and decreased RD in the splenium of the corpus
500 callosum. Using the mild LFP injury model, another study found decreased FA in the ipsilateral

501 corpus callosum at 3 and 5 days post-mTBI, and increased RD at day 5 post-mTBI (Wright et al.,
502 2016).

503 Consistent with our findings, a decrease in anisotropy and diffusivities in white matter were
504 also observed in humans in the acute phase of mTBI (Arfanakis et al., 2002; Inglese et al., 2005).
505 These studies reported decreased FA in the corpus callosum and internal capsule in the acute
506 phase in mTBI patients. Inglese and collaborators also demonstrated increased MD in the internal
507 capsule after mTBI (Inglese et al., 2005). In summary, findings from previous studies as well as the
508 present study reveal that major white matter areas are extensively damaged in the acute phase of
509 mTBI (Arfanakis et al., 2002; Inglese et al., 2005; Long et al., 2015; Wright et al., 2016; Li et al.,
510 2016; Tu et al., 2017; Herrera et al., 2017). In particular, our study demonstrated consistent
511 decreases in both anisotropy and diffusivities in the corpus callosum, external capsule, and
512 internal capsule.

513 Our findings in grey matter areas revealed decreased FA, AD, MD, and RD mainly in the
514 ipsilateral somatosensory and auditory cortices in the acute phase of mTBI. This is consistent with
515 the work of Wright and collaborators (Wright et al., 2016) who also demonstrated decreased AD
516 at 3 and 5 days post-mTBI in the ipsilateral cortex, and increased trace at day 3 post-mTBI. While
517 previous experimental and human studies revealed mainly white matter damage in the acute
518 phase of mTBI, our findings revealed damage in both white and grey matter areas at an acute
519 time-point.

520 Twenty-eight days after mTBI, voxel-wise group analysis revealed microstructural alterations
521 mainly in major white matter areas detected by *in vivo* DTI. We detected both decreased FA and
522 AD ipsilaterally in the corpus callosum and external capsule, and decreased FA in the internal
523 capsule in the subacute phase post-mTBI. In these white matter areas, the decreases in CL and CS
524 corroborated the decrease in FA at day 28 post-mTBI. Until now, only one study using a mild blast

525 injury model in rats reported changes in the DTI metrics at day 30 post-mTBI using *in vivo* DTI
526 (Budde et al., 2013). Laitinen and coworkers (Laitinen et al., 2015) using a severe form of the LFP
527 injury model also demonstrated microstructural tissue changes in white matter areas, which
528 included the genu of the corpus callosum, the angular bundle, and the internal capsule several
529 months after injury. Human studies also showed progressive changes in the DTI metrics in white
530 matter areas in the subacute phase in mild TBI patients (Rutgers et al., 2008; Messé et al., 2011).
531 Messé et al. (2011) reported higher MD values in the corpus callosum in the subacute phase of
532 mTBI between days 7 and 28 post-mTBI. In contrast, Rutgers and collaborators (Rutgers et al.,
533 2008) showed reduced FA predominantly in the corpus callosum and cingulum during the
534 subacute and chronic phases of mTBI. In accordance with previous experimental and human
535 studies, our results emphasize the persistent damage in white matter areas in the subacute phase
536 of mTBI.

537 **Volumetric changes in the brain after mTBI**

538 After TBI, neuronal damage induces anatomic as well as cellular morphology changes, leading to
539 neurodegeneration (Harris et al., 2019). Neurodegeneration is associated with progressive volume
540 loss after TBI detected by volumetric MRI measurements (Bigler, 2013; Cole et al., 2018). In our
541 study, we assessed volume changes using T2-weighted deformation-based morphometry analysis.
542 Our results revealed a volume reduction contralaterally in the lateral ventricle and ipsilaterally in
543 the ventrobasal complex, and increased volume in the external capsule and somatosensory cortex
544 in the acute phase of mTBI. Previous studies revealed that a volume increase might be associated
545 with edema early after mTBI (Mckee and Daneshvar, 2015; Stokum et al., 2016). In the subacute
546 phase of mTBI, our results mainly showed a progressive volume reduction in the grey matter such
547 as in the ipsilateral caudate putamen, hippocampus, ventrobasal complex, and cortical areas. In

548 white matter areas, we also observed a volume reduction in the corpus callosum, cingulum, and
549 internal capsule. After mTBI, a volume reduction in both white matter and grey matter areas is
550 commonly observed in humans, and might indicate neural or axonal degeneration (Bigler, 2013;
551 Mckee and Daneshvar, 2015). Until now, however, the few experimental studies that examined
552 volumetric changes after mTBI using MRI volumetric analysis in rats revealed no brain volume
553 changes (Kamnaksh et al., 2014; Wright et al., 2016). Kamnaksh and colleagues (Kamnaksh et al.,
554 2014), using DTI data in the mild blast injury model, reported no statistically significant volume
555 changes in the hippocampus. On the contrary, we assessed local morphometric changes using T2-
556 weighted images throughout the brain in the mild LFP injury model. Using the same animal model
557 as in our study, Wright and co-workers (Wright et al., 2016) did not find statistically significant
558 total volume changes in the cortex, hippocampus or corpus callosum using T2* data with ROI-
559 based analysis, however, we reported local morphometric changes in the cortex and subcortical
560 areas using T2 -weighted deformation based analysis.

561 In humans, the majority of studies that included MRI volumetric analysis performed after
562 moderate and severe TBI reported volumetric abnormalities in the cortex, thalamus, putamen,
563 and other regions (Gooijers et al., 2016; Cole et al., 2018). After mTBI, one human study also
564 reported a volume reduction in cortical areas at 1 month after mTBI (Toth et al., 2013). Although
565 Toth and collaborators (Toth et al., 2013) observed a volume loss in cortical areas in the subacute
566 phase of mTBI, they observed increased volume in the cortical grey matter, and decreased volume
567 in the ventricles and extracerebral cerebrospinal fluid at 3 days post-mTBI. We demonstrated a
568 volume reduction in white and grey matter areas, which progressed from the acute to the
569 subacute phase of mTBI, providing new insights in the detection of brain volume changes after
570 mTBI.

571 **Histology reveals axonal damage and gliosis that correlate with DTI after mTBI**

572 After the initial injury, an extensive complex cascade of molecular and cellular events occur,
573 referred to as secondary injury (Jassam et al., 2017). Secondary cellular mechanisms include
574 excitotoxicity and calcium flux, oxidative stress, mitochondrial dysfunction, and inflammation (Hill
575 et al., 2016). This extensive secondary injury leads to cell death, impaired synaptic plasticity, and
576 diffuse axonal injury, which compromise brain function (Walker and Tesco, 2013). Secondary
577 damage after TBI has been assessed using DTI and histologic examination (Rodriguez-Paez et al.,
578 2005; Mac Donald et al., 2007; Budde et al., 2011; Laitinen et al., 2015). To our knowledge, no
579 other study has examined these changes using quantitative histologic analysis targeted on the
580 basis of voxel-wise and morphologic MRI analyses. Previous studies demonstrated that decreased
581 FA and AD parameters are widely associated with axonal injury after TBI (Li et al., 2011; Mac
582 Donald et al., 2007; van de Looij et al., 2012). In the present study, we investigated the
583 contribution of axonal damage and gliosis to the decreased FA and AD in the subacute phase of
584 mTBI.

585 At 35 days post-mTBI, the most pronounced tissue changes were detected at the epicenter of
586 the lesion, but we also observed alterations far from the primary lesion. Specifically, rostral to the
587 lesion site, we detected axonal damage and increased cellularity (gliosis) in both white and grey
588 matter areas such as the corpus callosum, external capsule, and somatosensory cortex. The DTI
589 results correlated with the histologic parameters in the white matter, but not in the grey matter.
590 At the lesion site, a previous study using a mild LFP injury model reported axonal injury in white
591 and grey matter areas such as the corpus callosum, internal and external capsule, cingulum, and
592 thalamus on day 15 after mTBI (Hylin et al., 2013). That study, using both astrocyte and microglia
593 markers, also demonstrated inflammation in the corpus callosum and thalamus. Nevertheless, our
594 study demonstrated the presence of axonal damage and gliosis in white and grey matter regions

595 such as the corpus callosum, external capsule, internal capsule, somatosensory cortex, and ventral
596 posterolateral thalamic nucleus. This reveals the plausible contribution of both tissue components
597 to the decreases in FA and AD after mTBI. Notably, we found more extensive tissue changes in the
598 external capsule and somatosensory cortex compared with the above-mentioned areas in
599 association with the loss of myelinated axons. No alterations in the DTI metrics were found in the
600 somatosensory cortex by *in vivo* DTI, which might be related to the complexity of the structure.
601 Similar to the somatosensory cortex, *in vivo* DTI did not detect alterations in the ventral
602 posterolateral thalamic nucleus, although the histologic findings in this area revealed axonal
603 damage and gliosis. Nevertheless, our multiple linear regression test showed a correlation
604 between DTI and histology in both the white and grey matter, suggesting that both axonal damage
605 and cellularity may contribute to the DTI metrics. Furthermore, the correlations showed a greater
606 influence of the injury towards the primary lesion in the brain, consistent with our group analysis
607 results. These findings together demonstrate that axonal injury and gliosis contribute to the
608 alterations in DTI metrics in both the white and grey matter after mTBI.

609 **Technical limitations and future directions**

610 It is well known that the use of a simplistic tensor model in DTI underestimates the microstructure,
611 especially in morphologically complex areas such as the grey matter (Tournier et al., 2011), which
612 might explain the failure to detect mild microstructural changes in the somatosensory cortex and
613 ventral posterolateral thalamic nucleus in this study. Therefore, future studies should focus on
614 using more advanced diffusion MRI acquisitions and post-processing tools such as high-angular-
615 resolution diffusion imaging, diffusion kurtosis, q-ball imaging, and neurite orientation dispersion
616 and density imaging (Jensen et al., 2005; Kuo et al., 2008; Tournier et al., 2011; Zhang et al., 2012;
617 Douglas et al., 2015). To quantitatively assess the DTI findings, we used ST analysis as a sensitive

618 automated method offering anisotropy and orientation of histologic images equivalent to FA in
619 DTI (Budde and Frank, 2012). In the present study, we used 2D histologic sections limiting the
620 analysis to 2D, and therefore, missing the full 3D histopathologic interpretation. Future studies
621 should focus on using ST analysis of 3D histologic images acquired by advanced 3D microscopy
622 methods such as confocal, multi-photon, or electron microscopy (Schilling et al., 2016; Salo et al.,
623 2018; Abdollahzadeh et al., 2019).

624 It is important to highlight that this study uses only male rats and it may limit the translation of our
625 findings into the clinic (Rubin and Lipton, 2019). Therefore, future preclinical studies are needed to
626 assess the effect of sex on mTBI outcomes.

627

628 **Conclusion**

629 Our results indicate that *in vivo* DTI is sensitive for detecting widespread mild microstructural
630 tissue alterations in white and grey matter areas throughout the brain in the acute phase of mTBI.

631 In the subacute phase of mTBI, *in vivo* DTI detects progressive secondary tissue damage in the
632 white and grey matter at the lesion site, but fails to detect changes distal to the primary lesion.

633 We demonstrated that alterations in DTI metrics are associated with axonal damage and gliosis in
634 both the white and grey matter. These findings offer new insights for imaging progressive tissue
635 alterations after mTBI, highlighting the limitations of *in vivo* DTI for detecting mild microstructural
636 damage, but opening up new ways to investigate tissue damage after mTBI.

637

638 **References**

639 Abdollahzadeh A, Belevich I, Jokitalo E, Tohka J, Sierra A (2019) Automated 3D axonal
640 morphometry of white matter. *Sci Rep* 9:1–16.

- 641 Amyot F, Arciniegas DB, Brazaitis MP, Curley KC, Diaz-Arrastia R, Gandjbakhche A, Herscovitvh P,
642 Hinds II SR, Manley GT, Pacifico A, Razumovsky A, Riley J, Salzer W, Shih R, Smirniotopoulos
643 JG, Stockeer D (2015) A Review of the effectiveness of neuroimaging modalities for the
644 detection of traumatic brain injury. *J Neurotrauma* 32:1693–1721.
- 645 Andersson JLR, Sotiropoulos SN (2016) An integrated approach to correction for off-resonance
646 effects and subject movement in diffusion MR imaging. *Neuroimage* 125:1063–1078.
- 647 Arciniegas DB, Anderson CA, Topkoff J, McAllister TW (2005) Mild traumatic brain injury: a
648 neuropsychiatric approach to diagnosis, evaluation, and treatment. *Neuropsychiatr Dis Treat*
649 1:311–327.
- 650 Arfanakis K, Haughton VM, Carew JD, Rogers BP, Dempsey RJ, Meyerand ME (2002) Diffusion
651 tensor MR imaging in diffuse axonal injury. *Am Soc Neuroradiol* 23:794–802.
- 652 Avants BB, Epstein CL, Grossman M, Gee JC (2008) Symmetric diffeomorphic image registration
653 with cross-correlation: evaluating automated labeling of elderly and neurodegenerative
654 brain. *Med Image Anal* 12(1):26–41.
- 655 Avants BB, Tustison NJ, Song G, Cook PA, Klein A, Gee JC (2011) A reproducible evaluation of ANTs
656 similarity metrics performance in brain image registration. *Neuroimage* 54(3):2033–2044.
- 657 Basser PJ, Mattiello J, LeBihan D (1994) MR diffusion tensor spectroscopy and imaging. *Biophys J*
658 66:259–267.
- 659 Benjamini Y, Hochberg Y (1995) Controlling the false discovery rate: a practical and powerful
660 approach to multiple testing. *R Stat Soc* 57:289–300.
- 661 Bigler ED (2013) Traumatic brain injury, neuroimaging, and neurodegeneration. *Front Hum*
662 *Neurosci* 7:1–15.

- 663 Budde MD, Frank JA (2012) Examining brain microstructure using structure tensor analysis of
664 histological sections. *Neuroimage* 63:1–10.
- 665 Budde MD, Janes L, Gold E, Turtzo LC, Frank JA (2011) The contribution of gliosis to diffusion
666 tensor anisotropy and tractography following traumatic brain injury: validation in the rat
667 using Fourier analysis of stained tissue sections. *Brain* 134:2248–2260.
- 668 Budde MD, Shah A, McCrea M, Cullinan WE, Pintar FA, Stemper BD (2013) Primary blast traumatic
669 brain injury in the rat: relating diffusion tensor imaging and behavior. *Front Neurol* 4:1–12.
- 670 Chan TF, Vese LA (2001) Active contours without edges. *IEEE Trans Image Process* 10:266–277.
- 671 Cole JH, Jolly A, De Simoni S, Bourke N, Patel MC, Scott G, Sharp DJ (2018) Spatial patterns of
672 progressive brain volume loss after moderate-severe traumatic brain injury. *Brain* 141:822–
673 836.
- 674 Douglas DB, Iv M, Douglas PK, Anderson A, Vos SB, Bammer R, Zeineh M, Wintermark M (2015)
675 Diffusion tensor imaging of TBI: potentials and challenges. *Top Magn Reson Imaging* 24:241–
676 251.
- 677 Gardner RC, Yaffe K (2015) Epidemiology of mild traumatic brain injury and neurodegenerative
678 disease. *Mol Cell Neurosci* 66:75–80.
- 679 Gaser C, Nenadic I, Buchsbaum BR, Hazlett EA, Buchsbaum MS (2001) Deformation-based
680 morphometry and its relation to conventional volumetry of brain lateral ventricles in MRI.
681 *Neuroimage* 13:1140–1145.
- 682 Gooijers J, Chalavi S, Beeckmans K, Michiels K, Lafosse C, Sunaert S, Swinnen SP (2016) Subcortical
683 volume loss in the thalamus, putamen, and pallidum, induced by traumatic brain injury, is
684 associated with motor performance deficits. *Neurorehabil Neural Repair* 30:603–614.

- 685 Grandhi R, Tavakoli S, Ortega C, Simmonds MJ (2017) A review of chronic pain and cognitive,
686 mood, and motor dysfunction following mild traumatic brain injury: complex, comorbid,
687 and/or overlapping conditions? *Brain Sci* 7:1–8.
- 688 Harris TC, De Rooij R, Kuhl E (2019) The shrinking brain: cerebral atrophy following traumatic brain
689 injury. *Ann Biomed Eng* 47(9):1941–1959.
- 690 Herrera JJ, Bockhorst K, Kondraganti S, Stertz L, Quevedo J, Narayana PA (2017) Acute white
691 matter tract damage after frontal mild traumatic brain injury. *J Neurotrauma* 34:291–299.
- 692 Hill CS, Coleman MP, Menon DK (2016) Traumatic axonal injury: mechanisms and translational
693 opportunities. *Trends Neurosci* 39:311–324.
- 694 Hutchinson EB, Schwerin SC, Avram A V., Juliano SL, Pierpaoli C (2018) Diffusion MRI and the
695 detection of alterations following traumatic brain injury. *J Neurosci Res* 96:612–625.
- 696 Hylin MJ, Orsi SA, Zhao J, Bockhorst K, Perez A, Moore AN, Dash PK (2013) Behavioral and
697 histopathological alterations resulting from mild fluid percussion injury. *J Neurotrauma*
698 30:702–715.
- 699 Inglese M, Makani S, Johnson G, Cohen BA, Silver JA, Gonen O, Grossman RI (2005) Diffuse axonal
700 injury in mild traumatic brain injury: a diffusion tensor imaging study. *J Neurosurg* 103:298–
701 303.
- 702 Jassam YN, Izzy S, Whalen M, McGavern DB, El Khoury J (2017) Neuroimmunology of traumatic
703 brain injury: time for a paradigm shift. *Neuron* 95:1246–1265.
- 704 Jensen JH, Helpert JA, Ramani A, Lu H, Kaczynski K (2005) Diffusional kurtosis imaging: the
705 quantification of non-Gaussian water diffusion by means of magnetic resonance imaging.
706 *Magn Reson Med* 53:1432–1440.

- 707 Johnson VE, Stewart W, Smith DH (2013) Axonal pathology in traumatic brain injury. *Exp Neurol*
708 246:35–43.
- 709 Kamnaksh A, Budde MD, Kovesdi E, Long JB, Frank JA, Agoston DV (2014) Diffusion tensor imaging
710 reveals acute subcortical changes after mild blast-induced traumatic brain injury. *Sci Rep* 4:1–
711 6.
- 712 Kharatishvili I, Nissinen JP, McIntosh TK, Pitkänen A (2006) A model of posttraumatic epilepsy
713 induced by lateral fluid-percussion brain injury in rats. *Neuroscience* 140:685–697.
- 714 Kim JJ, Gean AD (2011) Imaging for the diagnosis and management of traumatic brain injury.
715 *Neurotherapeutics* 8:39–53.
- 716 Kinnunen KM, Greenwood R, Powell JH, Leech R, Hawkins PC, Bonnelle V, Patel MC, Counsell SJ,
717 Sharp DJ (2011) White matter damage and cognitive impairment after traumatic brain injury.
718 *Brain* 134:449–463.
- 719 Kuo LW, Chen JH, Wedeen VJ, Tseng WYI (2008) Optimization of diffusion spectrum imaging and q-
720 ball imaging on clinical MRI system. *Neuroimage* 41:7–18.
- 721 Laitinen T, Sierra A, Pitkänen A, Gröhn O (2010) Diffusion tensor MRI of axonal plasticity in the rat
722 hippocampus. *Neuroimage* 51:521–530.
- 723 Laitinen T, Sierra López A, Bolkvadze T, Pitkänen A, Gröhn O (2015) Diffusion tensor imaging
724 detects chronic microstructural changes in white and grey matter after traumatic brain injury
725 in rat. *Front Neurosci* 9:1–12.
- 726 Li J, Li XY, Feng DF, Gu L (2011) Quantitative evaluation of microscopic injury with diffusion tensor
727 imaging in a rat model of diffuse axonal injury. *Eur J Neurosci* 33:933–945.

- 728 Li W, Long JA, Watts L, Shen Q, Liu Y, Jiang Z, Duong TQ (2016) Spatiotemporal changes in
729 diffusion, T2 and susceptibility of white matter following mild traumatic brain injury. *NMR*
730 *Biomed* 29(7):896–903.
- 731 Long JA, Watts LT, Chemello J, Huang S, Shen Q, Duong TQ (2015) Multiparametric and
732 longitudinal MRI characterization of mild traumatic brain injury in rats. *J Neurotrauma*
733 32:598–607.
- 734 Mac Donald CL, Dikranian K, Song SK, Bayly P V., Holtzman DM, Brody DL (2007) Detection of
735 traumatic axonal injury with diffusion tensor imaging in a mouse model of traumatic brain
736 injury. *Exp Neurol* 205:116–131.
- 737 Marion CM, Radomski KL, Cramer NP, Galdzicki Z, Armstrong RC (2018) Experimental traumatic
738 brain injury identifies distinct early and late phase axonal conduction deficits of white matter
739 pathophysiology, and reveals intervening recovery. *J Neurosci* 38:8723–8736.
- 740 Mayer AR, Quinn DK, Master CL (2017) The spectrum of mild traumatic brain injury. *Neurology*
741 89:623–632.
- 742 McInnes K, Friesen CL, MacKenzie DE, Westwood DA, Boe SG (2017) Mild traumatic brain injury
743 (mTBI) and chronic cognitive impairment: a scoping review. *PLoS One* 12:1–19.
- 744 Mckee AC, Daneshvar DH (2015) The neuropathology of traumatic brain injury, 1st ed, Handbook
745 of Clinical Neurology. Elsevier B.V.
- 746 Messé A, Caplain S, Paradot G, Garrigue D, Mineo JF, Soto Ares G, Ducreux D, Vignaud F, Rozec G,
747 Desal H, Pélégriani-Issac M, Montreuil M, Benali H, Lehericy S (2011) Diffusion tensor imaging and
748 white matter lesions at the subacute stage in mild traumatic brain injury with persistent
749 neurobehavioral impairment. *Hum Brain Mapp* 32:999–1011.

- 750 Mori S, Zhang J (2006) Principles of diffusion tensor imaging and its applications to basic
751 neuroscience research. *Neuron* 51:527–539.
- 752 Mutch CA, Talbott JF, Gean A (2016) Imaging evaluation of acute traumatic brain injury. *Neurosurg*
753 *Clin N Am* 27:409–439.
- 754 Noble S, Scheinost D, Constable RT (2020) Cluster failure or power failure? evaluating sensitivity in
755 cluster-level inference. *Neuroimage* 209:116468.
- 756 Pajevic S, Pierpaoli C (1999) Color schemes to represent the orientation of anisotropic tissues from
757 diffusion tensor data: application to white matter fiber tract mapping in the human brain.
758 *Magn Reson Med* 42:526–540.
- 759 Pierpaoli C, Jezzard P, Basser PJ, Barnett A, Di Chiro G (1996) Diffusion tensor imaging of the
760 human brain. *Radiology* 637–648.
- 761 Rodriguez-Paez AC, Brunschwig JP, Bramlett HM (2005) Light and electron microscopic assessment
762 of progressive atrophy following moderate traumatic brain injury in the rat. *Acta Neuropathol*
763 109:603–616.
- 764 Rubin TG, Lipton ML (2019) Sex differences in animal models of traumatic brain injury. *J Exp*
765 *Neurosci* 13:1–10.
- 766 Rutgers DR, Toulgoat F, Cazejust J, Fillard P, Lasjaunias P, Ducreux D (2008) White matter
767 abnormalities in mild traumatic brain injury: a diffusion tensor imaging study. *Am J*
768 *Neuroradiol* 29:514–519.
- 769 Salo RA, Belevich I, Manninen E, Jokitalo E, Gröhn O, Sierra A (2018) Quantification of anisotropy
770 and orientation in 3D electron microscopy and diffusion tensor imaging in injured rat brain.
771 *Neuroimage* 172:404–414.

- 772 Schilling K, Janve V, Gao Y, Stepniewska I, Landman BA, Anderson AW (2016) Comparison of 3D
773 orientation distribution functions measured with confocal microscopy and diffusion MRI.
774 *Neuroimage* 129:185–197.
- 775 Shenton M, Hamoda H, Zafonte R (2012) A review of magnetic resonance imaging and diffusion
776 tensor imaging findings in mild traumatic brain injury. *Brain Imaging Behav* 6:137–192.
- 777 Sidaros A, Engberg AW, Sidaros K, Liptrot MG, Herning M, Petersen P, Paulson OB., Jernigan TL,
778 Rostrup E (2008) Diffusion tensor imaging during recovery from severe traumatic brain injury
779 and relation to clinical outcome: a longitudinal study. *Brain* 131:559–572.
- 780 Sierra A, Laitinen T, Gröhn O, Pitkänen A (2015) Diffusion tensor imaging of hippocampal network
781 plasticity. *Brain Struct Funct* 220:781–801.
- 782 Singh K, Trivedi R, Devi MM, Tripathi RP, Khushu S (2016) Longitudinal changes in the DTI
783 measures, anti-GFAP expression and levels of serum inflammatory cytokines following mild
784 traumatic brain injury. *Exp Neurol* 275:427–435.
- 785 Smith SM, Nichols TE (2009) Threshold-free cluster enhancement: addressing problems of
786 smoothing, threshold dependence and localisation in cluster inference. *Neuroimage* 44:83–
787 98.
- 788 Stokum JA, Gerzanich V, Simard JM (2016) Molecular pathophysiology of cerebral edema. *J Cereb*
789 *Blood Flow Metab* 36:513–538.
- 790 Tae WS, Ham BJ, Pyun SB, Kang SH, Kim BJ (2018) Current clinical applications of diffusion-tensor
791 imaging in neurological disorders. *J Clin Neurol* 14:129–140.
- 792 Toth A, Kovacs N, Perlaki G, Orsi G, Aradi M, Komaromy H, Ezer E, Bukovics P, Farkas O, Janszky J,
793 Doczi T, Buki A, Schwarcz A (2013) Multi-modal magnetic resonance imaging in the acute and

- 794 sub-acute phase of mild traumatic brain injury: can we see the difference? *J Neurotrauma*
795 30:2–10.
- 796 Tournier JD, Mori S, Leemans A (2011) Diffusion tensor imaging and beyond. *Magn Reson Med* 65
797 (6):1532–1556.
- 798 Tu TW, Lescher JD, Williams RA, Jikaria N, Turtzo LC, Frank JA (2017) Abnormal injury response in
799 spontaneous mild ventriculomegaly Wistar rat brains: a pathological correlation study of
800 diffusion tensor and magnetization transfer imaging in mild traumatic brain injury. *J*
801 *Neurotrauma* 34:248–256.
- 802 van de Looij Y, Mauconduit F, Beaumont M, Valable S, Farion R, Francony G, Payen JF, Lahrech H
803 (2012) Diffusion tensor imaging of diffuse axonal injury in a rat brain trauma model. *NMR*
804 *Biomed* 25:93–103.
- 805 Walker KR, Tesco G (2013) Molecular mechanisms of cognitive dysfunction following traumatic
806 brain injury. *Front Aging Neurosci* 5:1–25.
- 807 Westin CF, Maier SE, Mamata H, Nabavi A, Jolesz FA, Kikinis R (2002) Processing and visualization
808 for diffusion tensor MRI. *Med Image Anal* 6:93–108.
- 809 Winkler AM, Ridgway GR, Webster MA, Smith SM, Nichols TE (2014) Permutation inference for the
810 general linear model. *Neuroimage* 92:381–397.
- 811 Wright DK, Trezise J, Kamnaksh A, Bekdash R, Johnston LA, Ordidge R, Semple BD, Gardner AJ,
812 Stanwell P, O’Brien TJ, Agoston DV, Shultz SR (2016) Behavioral, blood, and magnetic
813 resonance imaging biomarkers of experimental mild traumatic brain injury. *Sci Rep* 6:1–16.
- 814 Yekutieli D, Benjamini Y (1999) Resampling-based false discovery rate controlling multiple test
815 procedures for correlated test statistics. *J Stat Plan Inference* 82:171–196.

816 Zhang H, Schneider T, Wheeler-Kingshott CA, Alexander DC (2012) NODDI: practical in vivo neurite
817 orientation dispersion and density imaging of the human brain. *Neuroimage* 61:1000–1016.

818 Zhuo J, Xu S, Proctor JL, Mullins RJ, Simon JZ, Fiskum G, Gullapalli RP (2012) Diffusion kurtosis as an
819 in vivo imaging marker for reactive astrogliosis in traumatic brain injury. *Neuroimage* 59:467–
820 477.

821

822 **Figure legends**

823 **Figure 1. ROIs included in the DTI analysis.** ROIs are outlined in a representative coronal FA map
824 of a sham-operated animal. Grey scale indicates FA values between 0 (black) and 1 (white).
825 Abbreviations: cc, corpus callosum; ec, external capsule; ic, internal capsule; S1, somatosensory
826 cortex; VPL, ventral posterolateral thalamic nucleus.

827

828 **Figure 2. Whole-brain voxel-wise group analysis of FA, AD, MD, and RD parameters comparing**
829 **sham-operated and mTBI animals at day 3.** The mTBI rats showed significantly reduced FA, AD,
830 MD, and RD parameters. The figure shows $1 - p$, where p is the permutation-based FWE corrected
831 p -value after TFCE enhancement of the test statistic; a corrected $p < 0.05$ was considered
832 significant (blue-light blue color scale). Abbreviations: AD, axial diffusivity; FA, fractional
833 anisotropy; MD, mean diffusivity; RD, radial diffusivity.

834

835 **Figure 3. Whole-brain voxel-wise group analysis of Westin's derived DTI parameters comparing**
836 **sham-operated and mTBI animals at 3 and 28 days.** The mTBI rats showed significantly reduced
837 Westin's derived DTI parameters. The figure shows $1 - p$, where p is the permutation-based FWE

838 corrected p -value after TFCE enhancement of the test statistic; a corrected $p < 0.05$ was
839 considered significant (blue-light blue color scale). Abbreviations: CL, linear anisotropy; CP, planar
840 anisotropy; CS, spherical anisotropy indices.

841

842 **Figure 4. Whole-brain voxel-wise group analysis of FA, AD, MD, and RD parameters comparing**
843 **sham-operated and mTBI animals at day 28.** The mTBI rats showed significantly reduced FA, AD,
844 MD, and AD parameters. The figure shows $1 - p$, where p is the permutation-based FWE corrected
845 p -value after TFCE enhancement of the test statistic; a corrected $p < 0.05$ was considered
846 significant (blue-light blue color scale). Abbreviations: AD, axial diffusivity; FA, fractional
847 anisotropy; MD, mean diffusivity; RD, radial diffusivity.

848

849 **Figure 5. Whole-brain group deformation-based morphometry analysis of T2-weighted images**
850 **comparing sham-operated and mTBI animals at day 3 (A) and 28 (B).** Brain volume differences
851 between sham-operated and mild TBI animals observed in acute and subacute phases post-mTBI.
852 The mTBI rats showed both volume enlargement (red-yellow color scale), and volume reduction
853 (blue-light blue color scale) compared with the sham-operated rats. The figure shows $1 - p$, where
854 p is the permutation-based FWE corrected p -value after TFCE enhancement of the test statistic; a
855 corrected $p < 0.05$ was considered significant.

856

857 **Figure 6. Representative whole-brain myelin-stained section of a sham-operated animal at +1.08**
858 **mm from bregma (A).** White squares in panel **A** indicate the location of high-magnification
859 photomicrographs of myelin- and Nissl-stained sections of a sham-operated (**i and iii**) and mTBI
860 animal (**ii and iv**) in the corpus callosum (**B**), external capsule (**C**), and somatosensory cortex (**D**).

861 The same animals are shown in both stainings. White arrowheads indicate axonal damage.
862 Abbreviations: cc, corpus callosum; ec, external capsule; S1, somatosensory cortex. Scale bars: 2
863 mm (A) and 50 μ m (B-D).

864

865 **Figure 7. Representative whole-brain myelin-stained section of a sham-operated animal at -1.60**
866 **mm from bregma (A).** White squares in panel A indicate the location of high-magnification
867 photomicrographs of myelin-stained sections and Nissl-stained sections of a sham-operated (i and
868 iii) and mTBI animal (ii and iv) in the corpus callosum (B), external capsule (C), and somatosensory
869 cortex (D). The same animals are shown in both stainings. White arrowheads indicate axonal
870 damage, and black arrowheads indicate gliosis shown by increased cellularity in Nissl-staining
871 sections. Abbreviations: cc, corpus callosum; ec, external capsule; S1, somatosensory cortex. Scale
872 bars: 2 mm (A) and 50 μ m (B-D).

873

874 **Figure 8. Representative whole-brain myelin-stained section of a sham-operated animal at -3.60**
875 **mm from bregma (A).** White squares in panel A indicate the location of high-magnification
876 photomicrographs of myelin-stained sections and Nissl-stained sections of a sham-operated (i and
877 iii) and mTBI animal (ii and iv) in the corpus callosum (B), external capsule (C), and somatosensory
878 cortex (D), internal capsule (E) and ventrobasal complex (F). The same animals are shown in both
879 stainings. White arrowheads indicate axonal damage, and white arrows point to loss of myelinated
880 axons. Black arrowheads indicate gliosis shown by increased cellularity in Nissl-staining sections.
881 Abbreviations: cc, corpus callosum; ec, external capsule; ic, internal capsule; S1, somatosensory
882 cortex; VPL, ventral posterolateral thalamic nucleus. Scale bars: 2 mm (A) and 50 μ m (B-F).

883

884 **Figure 9. Representative multiple linear regression analyses of quantitative DTI and histological**
885 **analysis parameters at +1.08 mm (A and B), -1.60 mm (C and D), and -3.60 mm (E, F, G and H)**
886 **from bregma.** The thick black line is the regression line, and the two thin dotted lines represent
887 the 95% confidence interval. Both sham-operated and mTBI animals (ipsi- and contralateral
888 hemispheres) are represented by colors, and the brain areas by shapes. The X-axis represents the χ
889 values obtained with the expression: $\chi = \beta_{AI} \times AI + \beta_{CD} \times CD$, where β is the weighting value. The Y-
890 axis represents FA or AD ($\times 10^{-3} \text{ mm}^2/\text{s}$). CD values are scaled ($\times 10^{-2} \text{ cell}/\mu\text{m}^2$). Abbreviations: AD,
891 axial diffusivity; AI, anisotropy index; cc, corpus callosum; CD, cell density; ec, external capsule; FA,
892 fractional anisotropy; ic, internal capsule; S1, somatosensory cortex; VPL, ventral posterolateral
893 thalamic nucleus.

894

895 **Table 1. Quantitative histologic analysis at +1.08 mm, -1.60 mm and -3.60 mm from bregma.**

896 Statistically significant FDR-corrected q -values are shown ($*q$ -value < 0.05 corresponding to
897 uncorrected $*p$ -value $< 3.10 \times 10^{-3}$; unpaired t-test) for the anisotropy index (AI) and cell density
898 (CD) ($\times 10^{-2} \text{ cell}/\mu\text{m}^2$). Abbreviations: AI, anisotropy index; cc, corpus callosum; CD, cell density; ec,
899 external capsule; ic, internal capsule; S1, somatosensory cortex; VPL, ventral posterolateral
900 thalamic nucleus.

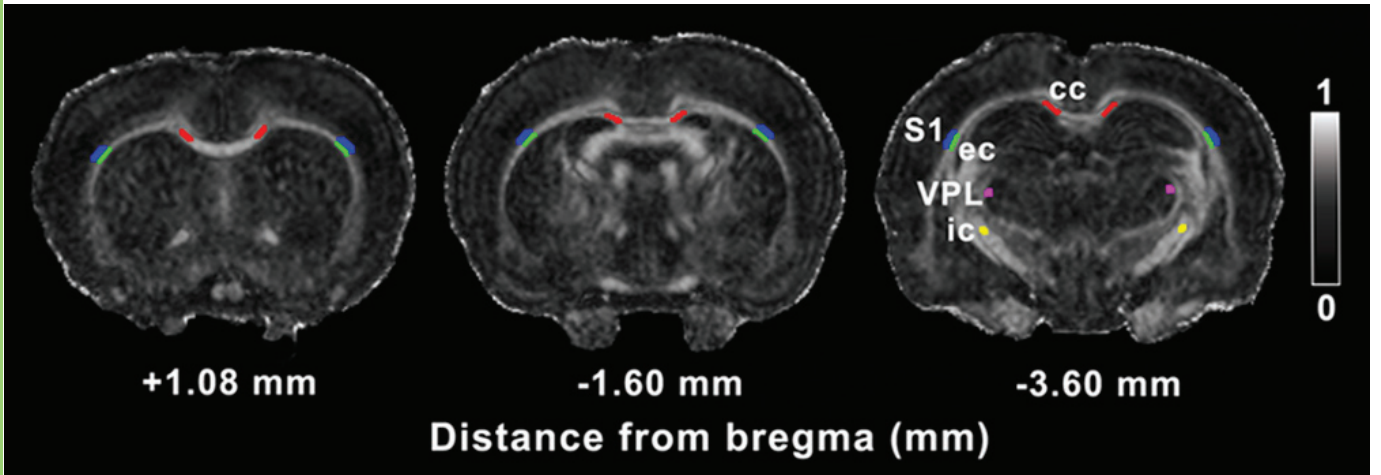
901

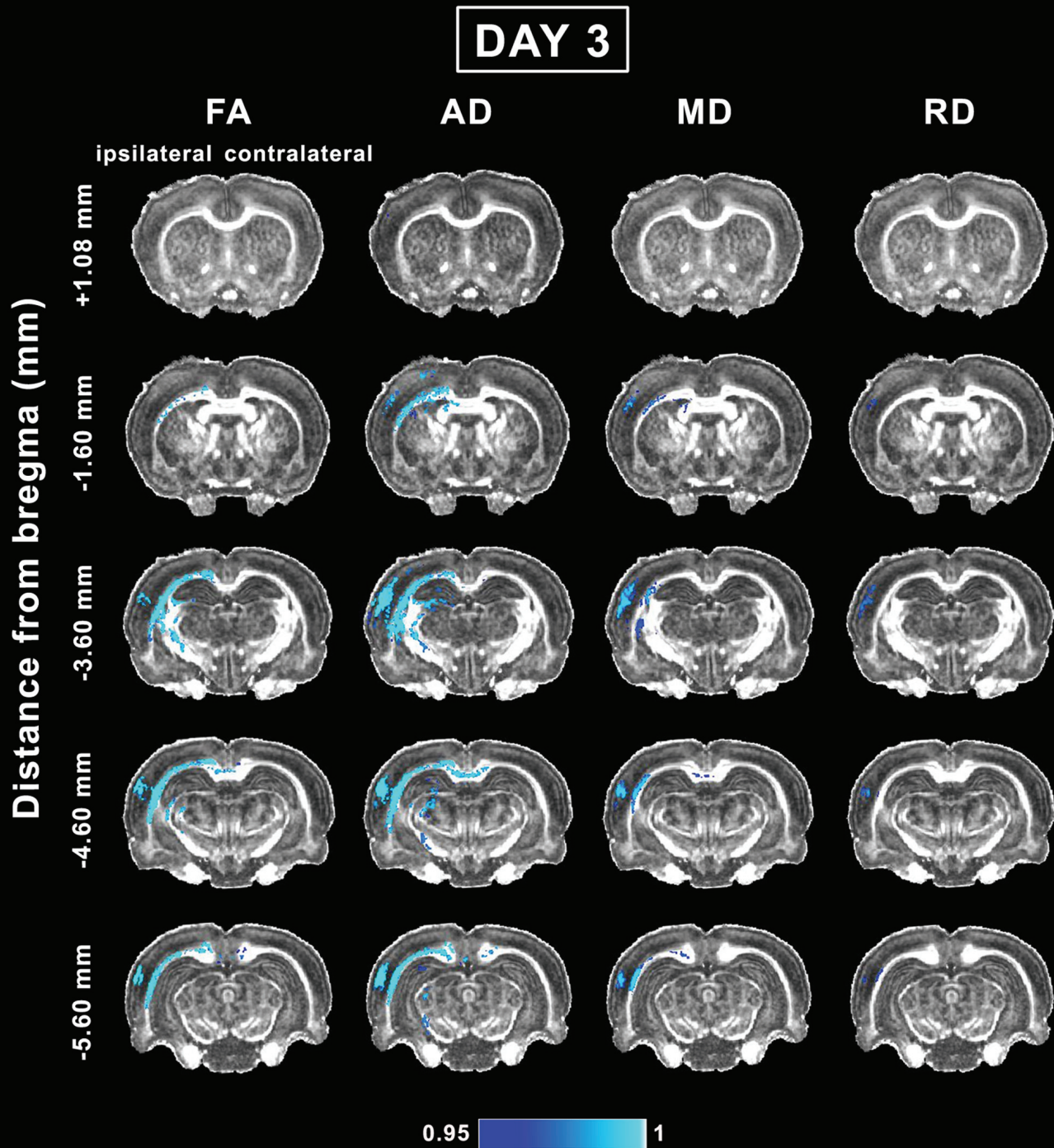
902 **Table 2. Multiple linear regression between quantitative DTI and histologic analysis at +1.08**

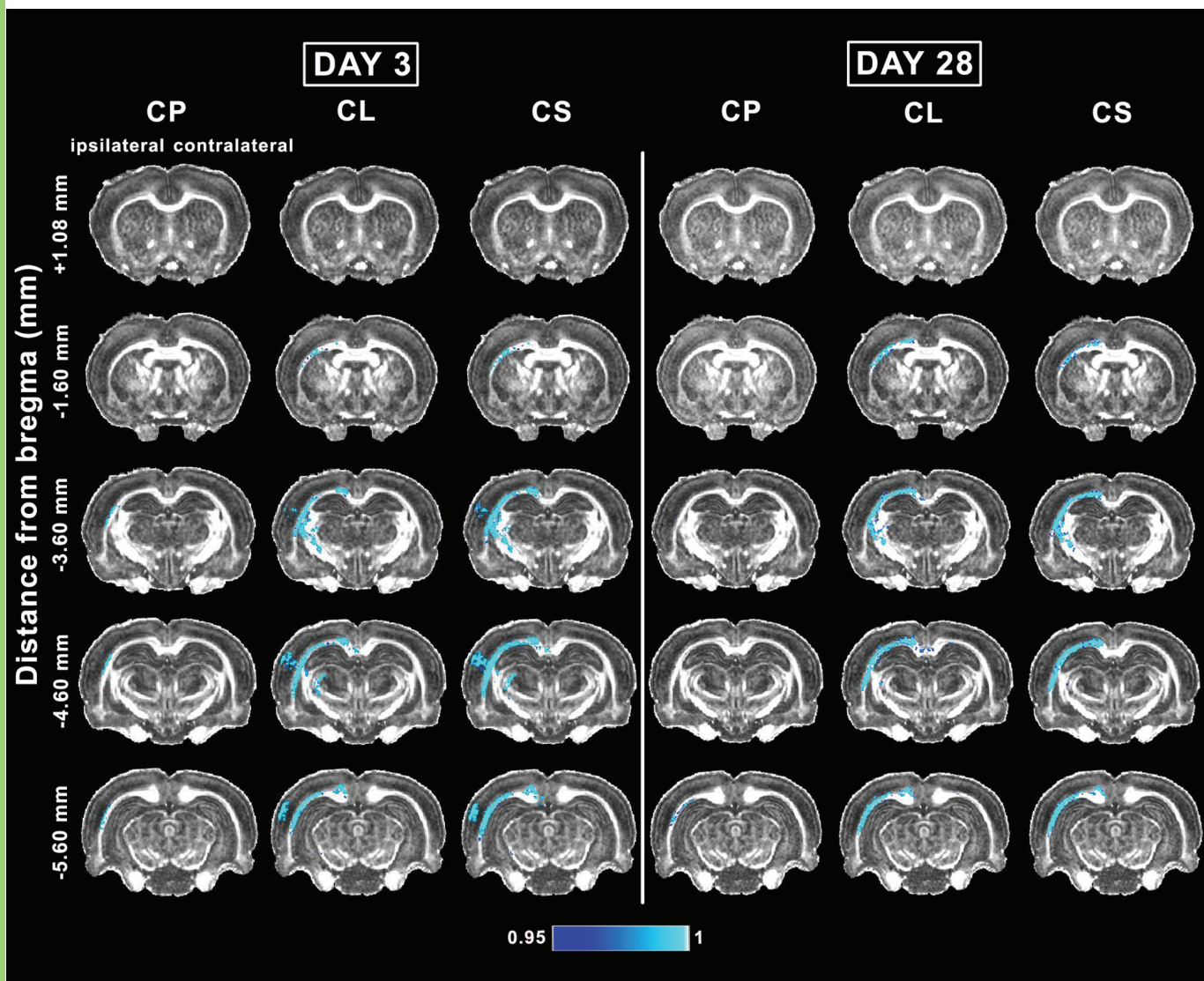
903 **mm, -1.60 mm, and -3.60 mm from bregma.** Statistically significant FDR-corrected q -values are
904 shown ($*q$ -value < 0.05 ; $**q$ -value < 0.01 ; $***q$ -value < 0.001 corresponding to uncorrected $*p$ -
905 value $< 1.97 \times 10^{-2}$; $**p$ -value $< 2.5 \times 10^{-3}$; $***p$ -value $< 1.22 \times 10^{-4}$, respectively; Multiple linear
906 regression test) for the anisotropy index (AI), cell density (CD) ($\times 10^{-2} \text{ cell}/\mu\text{m}^2$), and both

907 parameters. Abbreviations: AD, axial diffusivity; AI, anisotropy index; cc, corpus callosum; CD, cell
908 density; ec, external capsule; FA, fractional anisotropy; ic, internal capsule; S1, somatosensory
909 cortex; VPL, ventral posterolateral thalamic nucleus.

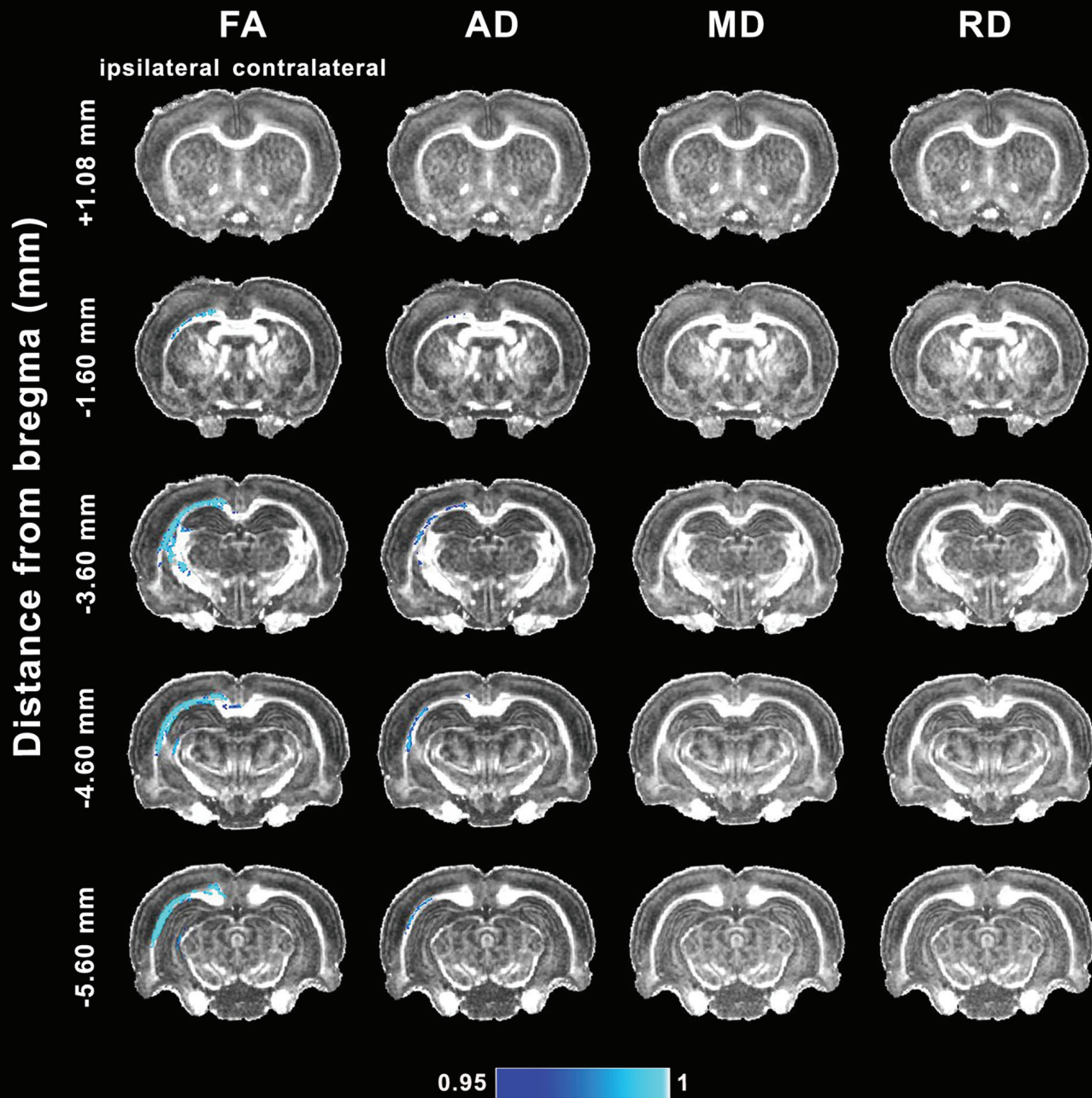
910

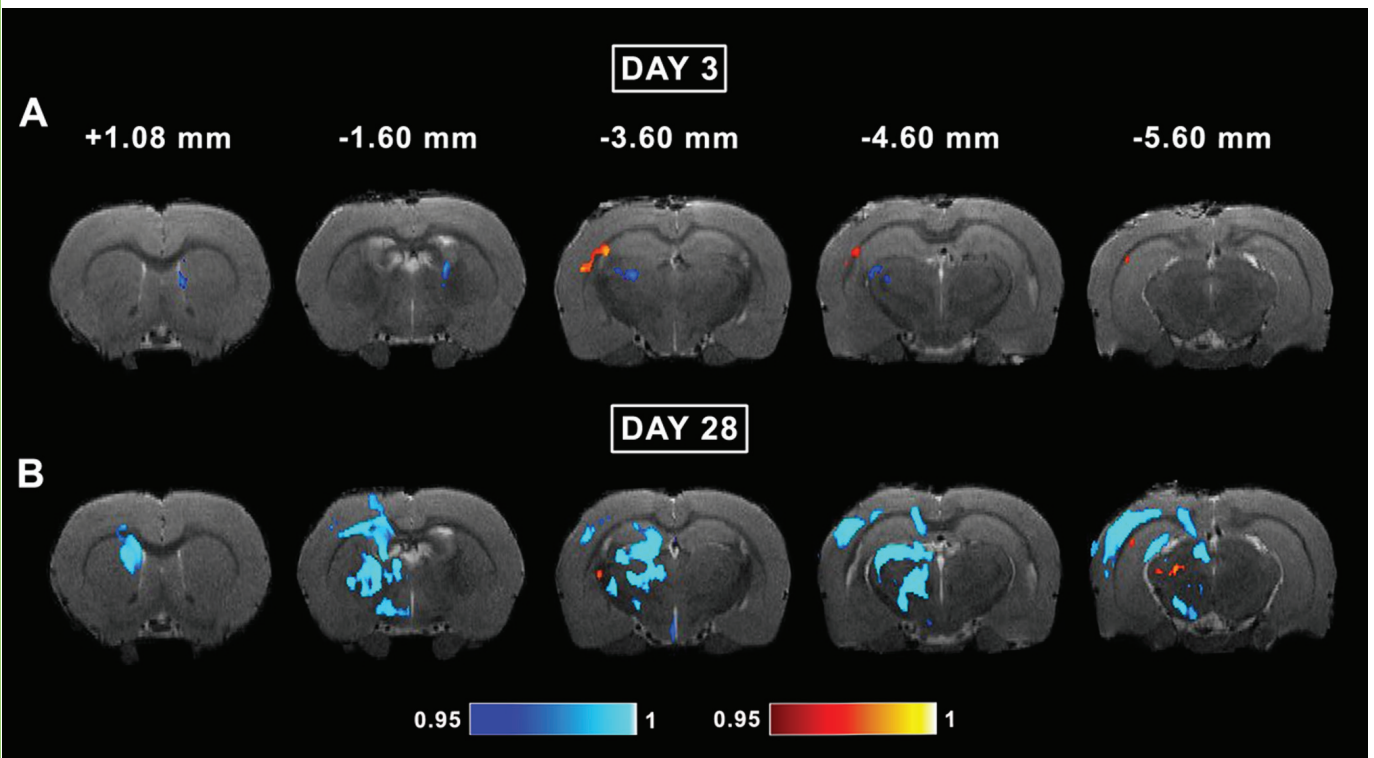


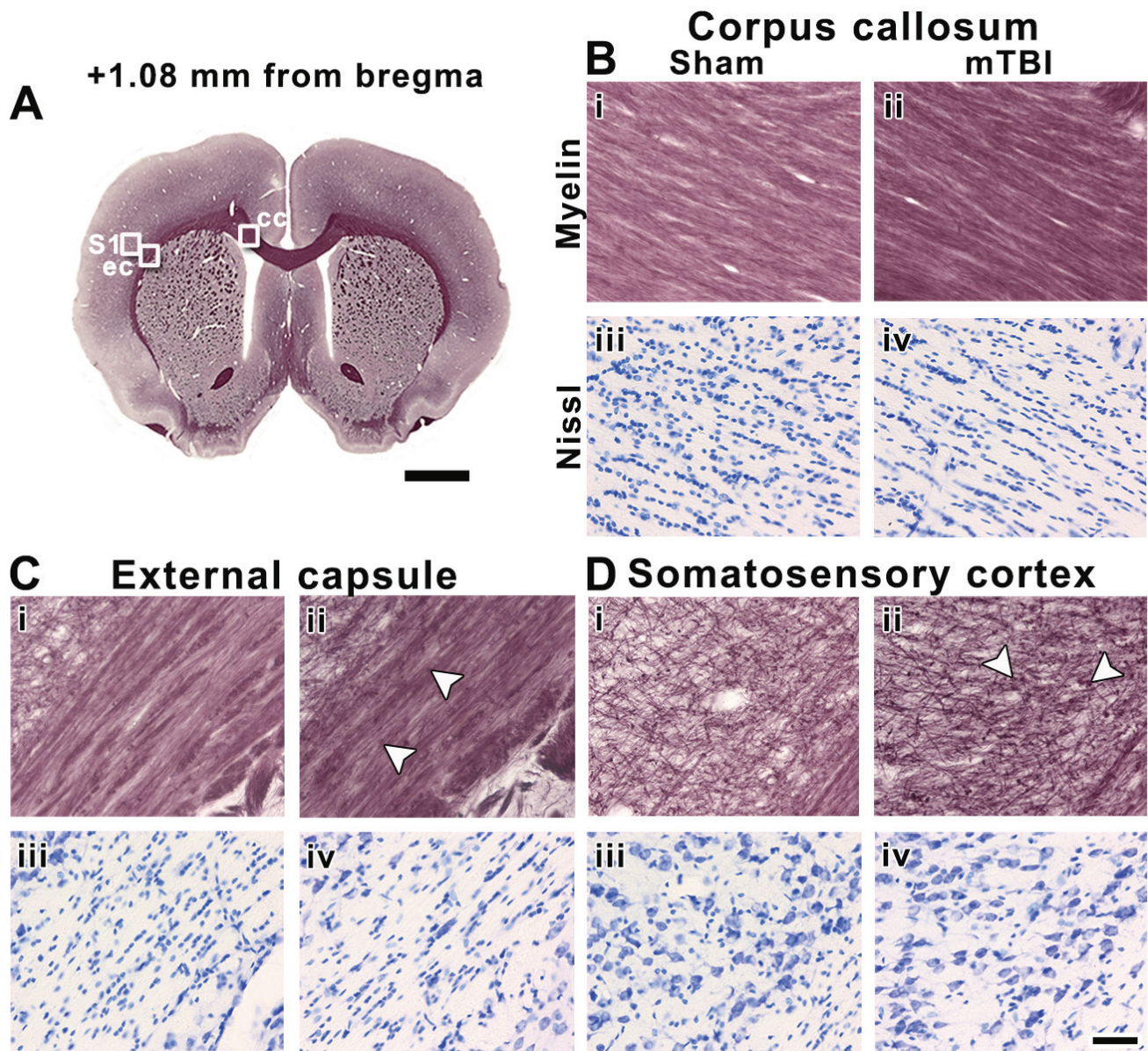


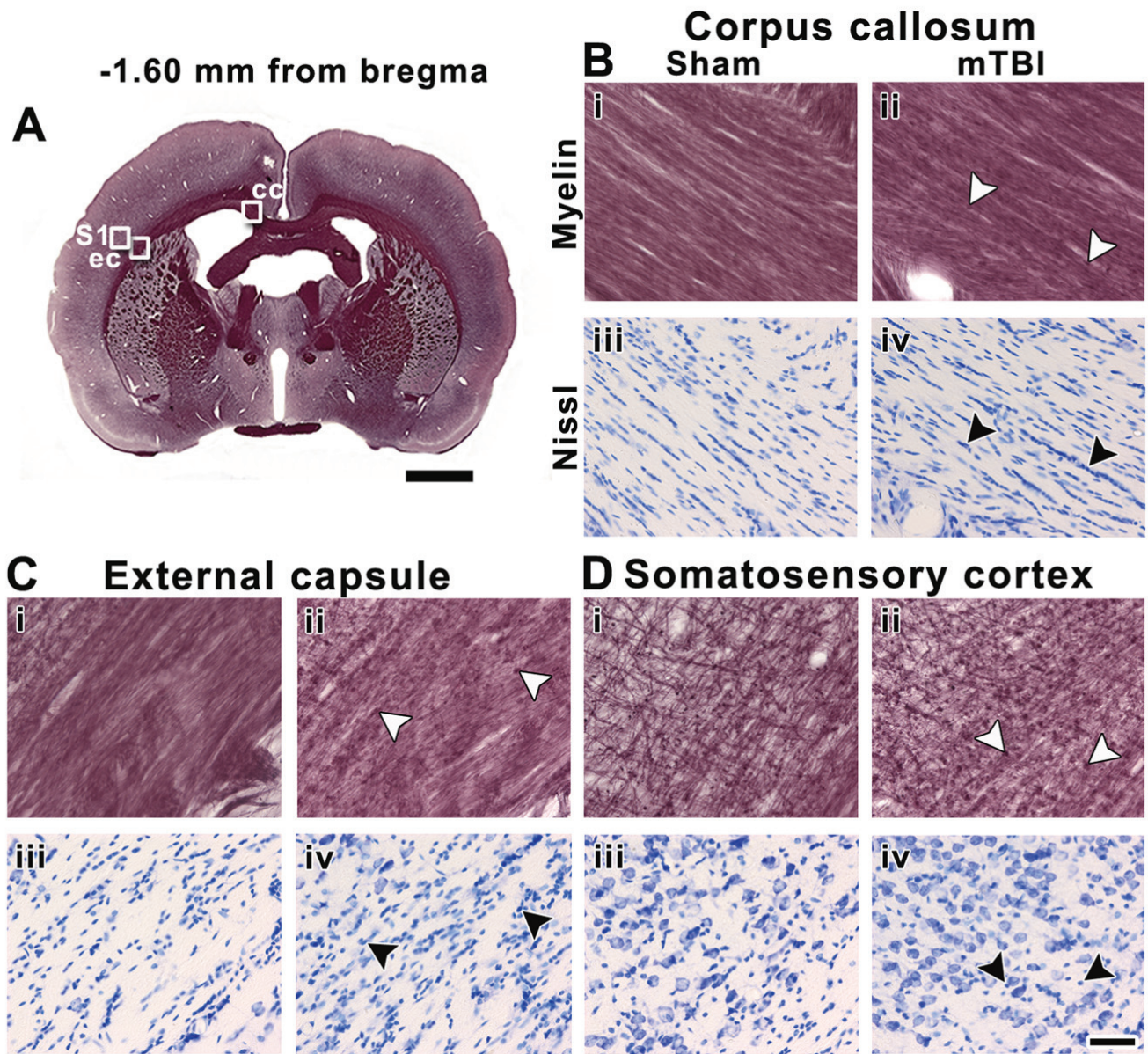


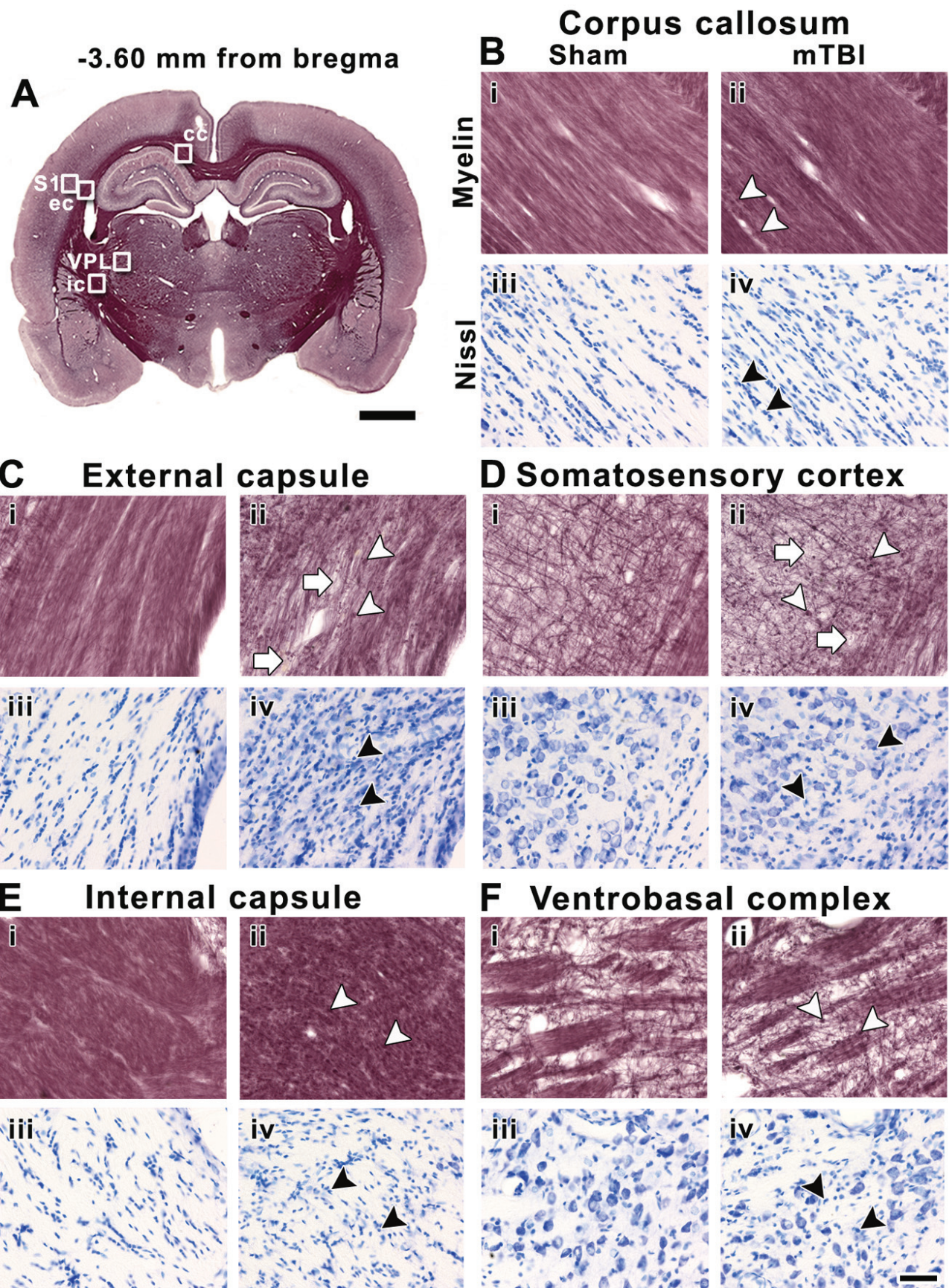
DAY 28











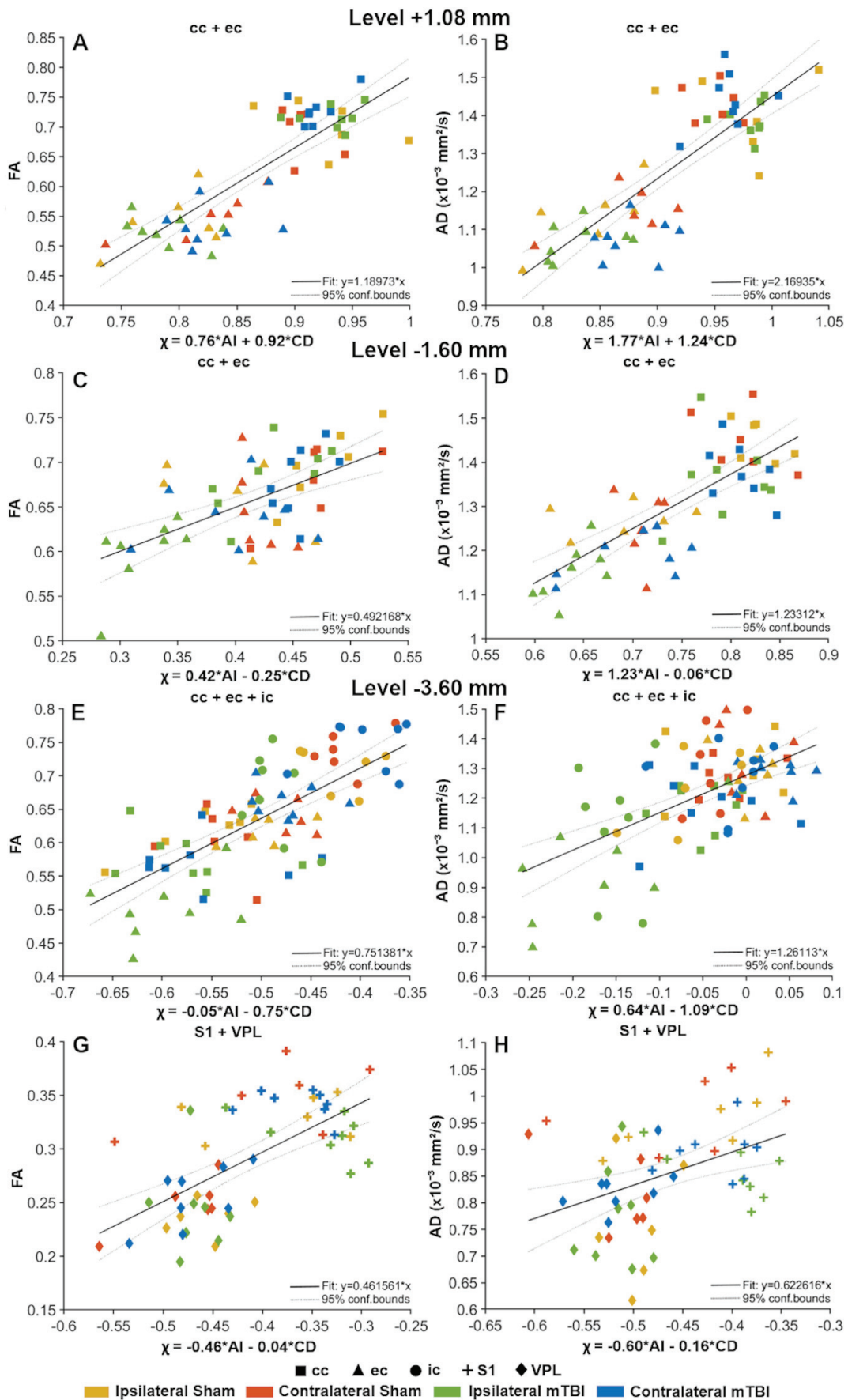


Table 1. Quantitative histologic analysis at +1.08 mm, -1.60 mm and -3.60 mm from bregma.

Level +1.08 mm									
t-test	Ipsilateral					Contralateral			
	AI		CD (x 10 ⁻² cell/μm ²)			AI		CD (x 10 ⁻² cell/μm ²)	
	Mean ± SD	t (AI)	Mean ± SD	t (CD)	Mean ± SD	t (AI)	Mean ± SD	t (CD)	
cc	Sham	0.81 ± 0.05	0.61	0.53 ± 0.03	0.41	0.80 ± 0.04	0.51	0.52 ± 0.04	0.38
	mTBI	0.83 ± 0.03		0.52 ± 0.04		0.81 ± 0.03		0.52 ± 0.02	
ec	Sham	0.73 ± 0.04	0.94	0.43 ± 0.03	0.62	0.75 ± 0.03	0.25	0.44 ± 0.05	0.47
	mTBI	0.71 ± 0.04		0.44 ± 0.04		0.75 ± 0.03		0.46 ± 0.05	
S1	Sham	0.43 ± 0.06	1.06	0.39 ± 0.02	0.56	0.47 ± 0.04	0.11	0.39 ± 0.01	0.80
	mTBI	0.47 ± 0.06		0.40 ± 0.06		0.47 ± 0.01		0.38 ± 0.03	
Level -1.60 mm									
cc	Sham	0.85 ± 0.02	2.06	0.51 ± 0.05	1.46	0.84 ± 0.04	0.04	0.50 ± 0.02	1.89
	mTBI	0.82 ± 0.04		0.55 ± 0.04		0.82 ± 0.03		0.53 ± 0.03	
ec	Sham	0.71 ± 0.06	1.91	0.43 ± 0.04	2.91	0.73 ± 0.02	0.51	0.42 ± 0.03	1.22
	mTBI	0.66 ± 0.03		0.50 ± 0.05		0.72 ± 0.05		0.44 ± 0.04	
S1	Sham	0.38 ± 0.05	0.23	0.39 ± 0.02	1.18	0.45 ± 0.05	0.52	0.39 ± 0.02	0.45
	mTBI	0.38 ± 0.06		0.41 ± 0.03		0.44 ± 0.05		0.39 ± 0.02	
Level -3.60 mm									
cc	Sham	0.83 ± 0.04	1.18	0.50 ± 0.06	0.50	0.80 ± 0.06	1.25	0.49 ± 0.03	0.37
	mTBI	0.78 ± 0.05		0.52 ± 0.06		0.75 ± 0.07		0.50 ± 0.06	
ec	Sham	0.76 ± 0.03	4.97	0.44 ± 0.03	4.71	0.73 ± 0.04	2.44	0.43 ± 0.03	0.47
	mTBI	0.60 ± 0.08*		0.56 ± 0.06*		0.78 ± 0.03		0.42 ± 0.03	
S1	Sham	0.34 ± 0.07	1.40	0.39 ± 0.02	4.01	0.35 ± 0.09	0.63	0.39 ± 0.03	1.04
	mTBI	0.30 ± 0.05		0.46 ± 0.05*		0.33 ± 0.04		0.38 ± 0.01	
ic	Sham	0.53 ± 0.09	1.40	0.38 ± 0.03	4.23	0.56 ± 0.08	0.23	0.38 ± 0.02	1.19
	mTBI	0.47 ± 0.04		0.45 ± 0.02*		0.57 ± 0.04		0.35 ± 0.04	
VPL	Sham	0.43 ± 0.03	0.49	0.33 ± 0.03	3.08	0.45 ± 0.05	0.28	0.33 ± 0.03	0.30
	mTBI	0.43 ± 0.03		0.38 ± 0.04		0.44 ± 0.04		0.34 ± 0.03	

Statistically significant FDR-corrected *q*-values are shown (**q*-value < 0.05 corresponding to uncorrected **p*-value < 3.10 × 10⁻³; unpaired t-test) for the anisotropy index (AI) and cell density (CD) (x 10⁻² cell/μm²). Abbreviations: AI, anisotropy index; cc, corpus callosum; CD, cell density; ec, external capsule; ic, internal capsule; S1, somatosensory cortex; VPL, ventral posterolateral thalamic nucleus.

Table 2. Multiple linear regression between quantitative DTI and histologic analysis at +1.08 mm, -1.60 mm and -3.60 mm from bregma.

Level +1.08 mm								
	FA				AD ($\times 10^{-3}$ mm ² /s)			
	R ² adj	F-stat	t(AI)	t(CD)	R ² adj	F-stat	t(AI)	t(CD)
cc	0.02	1.24	-1.42	0.14	0	0.46	-0.20	-0.94
ec	0.11	2.64	1.38	1.88	0.15	3.45	2.58*	0.58
S1	0.01	1.09	-0.11	1.47	0	0.15	-0.16	-0.48
cc + ec	0.68***	60.0	5.10***	6.28***	0.66***	55.1	6.34***	4.53***
Level -1.60 mm								
cc	0.51***	14.8	1.49	-4.97***	0.09	2.25	-0.42	-2.12
ec	0.08	2.14	0.14	-1.94	0.25*	5.52	2.08	-1.87
S1	0	0.40	0.66	-0.55	0.05	1.65	-0.98	-1.60
cc + ec	0.33***	14.5	5.39***	-2.40	0.55***	34.3	7.54***	-0.28
Level -3.60 mm								
cc	0.20	4.29	2.91*	-0.78	0	0.87	1.17	-0.79
ec	0.72***	35.4	3.00*	-2.37	0.69***	31.4	4.54***	-0.32
S1	0.08	2.19	-0.35	-2.06	0.03	1.47	-0.36	0.10
ic	0.23*	4.95	1.98	-1.51	0.33**	7.76	3.72**	0.19
VPL	0.15	3.37	-1.96	-2.03	0	0.59	0.28	-0.98
cc + ec	0.53***	32.0	5.02***	-4.63***	0.48***	26.5	5.45***	-3.17**
cc + ec + ic	0.51***	44.2	-1.09	-8.52***	0.33***	21.6	5.44***	-5.23***
S1 + VPL	0.39***	18.6	-5.12***	-0.33	0.14*	5.48	-2.95*	-0.52

Statistically significant FDR-corrected q -values are shown (* q -value < 0.05; ** q -value < 0.01; *** q -value < 0.001 corresponding to uncorrected * p -value < 1.97×10^{-2} ; ** p -value < 2.5×10^{-3} ; *** p -value < 1.22×10^{-4} , respectively; Multiple linear regression test) for the anisotropy index (AI), cell density (CD) ($\times 10^{-2}$ cell/ μm^2), and both parameters. Abbreviations: AD, axial diffusivity; AI, anisotropy index; cc, corpus callosum; CD, cell density; ec, external capsule; FA, fractional anisotropy; ic, internal capsule; S1, somatosensory cortex; VPL, ventral posterolateral thalamic nucleus.